Monthly Notices of the ROYAL ASTRONOMICAL SOCIETY

MNRAS **514,** 2527–2544 (2022) https://doi.org/10.1093/mnras/stac1498
Advance Access publication 2022 June 7

Age determination of galaxy merger remnant stars using asteroseismology

Camilla C. Borre [1]★ Víctor Aguirre Børsen-Koch,[1] Amina Helmi,[2] Helmer H. Koppelman,[3] Martin B. Nielsen [4], Jakob L. Rørsted [1]★ Dennis Stello,[1,5,6,7] Amalie Stokholm [1,8] Mark L. Winther,[1] Guy R. Davies,[4] Marc Hon,[9] J. M. Diederik Kruijssen [10], Chervin F. P. Laporte [11], Claudia Reyes[5] and Jie Yu [12]

[1]*Stellar Astrophysics Centre, Department of Physics and Astronomy, Aarhus University, Ny Munkegade 120, DK-8000 Aarhus C, Denmark*
[2]*Kapteyn Astronomical Institute, University of Groningen, Landleven 12, NL-9747 AD Groningen, the Netherlands*
[3]*School of Natural Sciences, Institute for Advanced Study, 1 Einstein Drive, Princeton, NJ 08540, USA*
[4]*School of Physics and Astronomy, University of Birmingham, Birmingham B15 2TT, UK*
[5]*School of Physics, The University of New South Wales, Sydney, NSW 2052, Australia*
[6]*ARC Centre of Excellence for Astrophysics in Three Dimensions (ASTRO-3D), Australia*
[7]*Sydney Institute for Astronomy (SIfA), School of Physics, University of Sydney, Sydney, NSW 2006, Australia*
[8]*Dipartimento di Fisica e Astronomia, Università degli Studi di Bologna, Via Gobetti 93/2, I-40129 Bologna, Italy*
[9]*Institute for Astronomy, University of Hawai'i, 2680 Woodlawn Drive, Honolulu, HI 96822, USA*
[10]*Astronomisches Rechen-Institut, Zentrum für Astronomie der Universität Heidelberg, Mönchhofstraße 12-14, D-69120 Heidelberg, Germany*
[11]*Institut de Ciencies del Cosmos (ICCUB), Universitat de Barcelona (IEEC-UB), Martíi i Franques 1, E-08028 Barcelona, Spain*
[12]*Max-Planck-Institut für Sonnensystemforschung, Justus-von-Liebig-Weg 3, D-37077 G'ottingen, Germany*

Accepted 2022 May 26. Received 2022 May 26; in original form 2021 November 2

ABSTRACT

The Milky Way was shaped by the mergers with several galaxies in the past. We search for remnant stars that were born in these foreign galaxies and assess their ages in an effort to put upper limits on the merger times and thereby better understand the evolutionary history of our Galaxy. Using 5D-phase space information from *Gaia* eDR3, radial velocities from *Gaia* DR2 and chemical information from APOGEE DR16, we kinematically and chemically select 21 red giant stars belonging to former dwarf galaxies that merged with the Milky Way. With added asteroseismology from *Kepler* and *K2* , we determine the ages of the 21 *ex situ* stars and 49 *in situ* stars with an average $\sigma_{\rm age}$/age of ∼31 per cent. We find that all the *ex situ* stars are consistent with being older than 8 Gyr. While it is not possible to associate all the stars with a specific dwarf galaxy, we classify eight of them as Gaia-Enceladus/Sausage stars, which is one of the most massive mergers in our Galaxy's history. We determine their mean age to be 9.5 ± 1.3 Gyr consistent with a merger time of 8–10 Gyr ago. The rest of the stars are possibly associated with Kraken, Thamnos, Sequoia, or another extragalactic progenitor. The age determination of *ex situ* stars paves the way to more accurately pinning down when the merger events occurred and hence provide tight constraints useful for simulating how these events unfolded.

Key words: asteroseismology – stars: abundances – stars: kinematics and dynamics – Galaxy: evolution.

1 INTRODUCTION

In the age of large stellar surveys such as *Gaia* (Gaia Collaboration 2016, 2021) and APOGEE (Majewski et al. 2017), it becomes increasingly possible to investigate our Galaxy, the Milky Way, in great detail. Knowledge of the stars' motion on the sky and their chemical compositions provides us with tools to examine where the stars originated. With precise age determination of single stars, we can contribute to the mapping of the evolution and history of the Galaxy. Using the properties of stars to infer properties of the Galaxy is known as Galactic archaeology (Freeman & Bland-Hawthorn 2002).

One of the goals of Galactic archaeology is to study the merger history of our Galaxy. Large galaxies like and including the Milky Way are expected to have merged with several dwarf galaxies throughout their lifetimes (see e.g. Helmi et al. 1999; Bell et al. 2008; Koppelman et al. 2019; Elias et al. 2020; Kruijssen et al. 2020; Naidu et al. 2020). Remnants of such a merger in the Milky Way was found by Helmi et al. (2018) using the *Gaia* data release 2 (DR2; Gaia Collaboration 2016, 2018) and chemical information from APOGEE (Majewski et al. 2017). The merger was also proposed by Belokurov et al. (2018) who used *Gaia* DR1 dynamical information. Both groups found stars that are kinematically different to the majority of the Milky Way stars and Helmi et al. (2018) furthermore demonstrated that they are also chemically different. The differences in kinematics and chemistry were attributed to them not being born *in situ* with the rest of the Milky Way stars but rather *ex situ* in a separate dwarf galaxy that had merged with the Milky Way. The dwarf galaxy was named Gaia-Enceladus by Helmi et al. (2018) and Gaia-Sausage by Belokurov et al. (2018) and we will refer to it as Gaia-Enceladus-Sausage or GES throughout this work.

Several other merger galaxies have been discovered since GES, although there are still debate as to which galaxies are unique galaxies and which are part of other already known galaxies (for a discussion

★ E-mail: cborre@phys.au.dk (CCB); jakob@phys.au.dk (JLR)

on this, see e.g. Helmi 2020). Other such merged galaxies are Sequoia (Myeong et al. 2019), Thamnos (Koppelman et al. 2019), and Kraken (Kruijssen et al. 2020) to name a few. Because GES is one of the most massive and mainly where the stars in this work appear to originate from (see Section 5.2.1), we will primarily focus on GES in this work.

From kinematics, the GES stars (and many *ex situ* stars in general) distinguish themselves from the Milky Way stars by being mainly found in the halo, meaning they are not very tightly bound in the Galactic potential and some are even on slightly retrograde orbits. Koppelman, Bos & Helmi (2020) used simulations by Villalobos & Helmi (2008) of collisions between a Milky Way-like galaxy and a GES -like dwarf galaxy with (i) different orbital inclinations and prograde/retrograde configurations and (ii) different types of progenitors (disky and spherical) to demonstrate that a counter-rotating dwarf spiral galaxy with an in-fall angle of 30°, relative to the Milky Way disc, would produce a final product with stellar dynamics very close to what we observe for GES today. During the collision, the dynamics of the stars in the Milky Way and GES were both perturbed but the original counter-rotating signature of GES can still be seen in some present-day halo stars (Helmi et al. 2018). In general, most *ex situ* stars will have a different dynamical signature than *in situ* stars but because several of the *in situ* stars were also perturbed during the merger, the dynamics alone is not enough to distinguish *in situ* from *ex situ* stars; however, chemical compositions can provide us with another diagnostic tool (Jean-Baptiste et al. 2017).

Nissen & Schuster (2010) were one of the first to show that there are two chemically distinct populations in the Milky Way halo, which was one of the first indications of a different galaxy being embedded in our Milky Way. The chemical evolution of the interstellar medium – and thereby the surface abundance of newborn stars – is predominantly governed by the rate and types of supernovae explosions, which in turn is controlled by the star formation rate (SFR) of the host galaxy. Simply put, there are two main types of supernovas produced by either massive stars ($\gtrsim$8 $M_\odot$) or low-mass stars. Massive stars have shorter lifetimes and explode as core-collapse supernovas or *Type II supernovae* (SNII). This kind of SNII produces large amounts of α-elements such as O, Mg, Si, S, Ca, and Ti as well as other elements such as Na and Al. Once the longer lived lower mass stars have had time to evolve to white dwarfs they can – if they are in a binary system – collide with another white dwarf companion to produce a *Type Ia supernova* (SNIa; Whelan & Iben 1973; Iben & Tutukov 1991; Kromer et al. 2015). The SNIa releases very small amounts of α-elements but large amounts of for example iron. When the occurrence rate of SNIa increases the α-element content of the interstellar medium stays mostly constant while the [Fe/H] content increases. As [α/Fe] depends on the amount of iron released in the interstellar medium, [α/Fe] will decrease when the SNIa sets in. This produces a bend in the [α/Fe] versus [Fe/H] relation with [α/Fe] being constant early in the galaxy's lifetime and later decreasing as [Fe/H] increases. Where this bend or 'knee' occurs depends on the mass and SFR in the galaxy (see e.g. Howell et al. 2014; Helmi et al. 2018). Massive galaxies have more gas than less massive galaxies and can form several generations of stars throughout its life. Davé (2008) shows a tight relation between galaxy mass and SFR up till $z \sim 2$. Smaller dwarf galaxies that have less gas have a smaller SFR and the onset of SNIa explosions happens at a lower [Fe/H] abundance. The stars from smaller galaxies therefore have a lower [Fe/H] abundance at the same [α/Fe] abundance compared to stars in a more massive galaxy. In the literature, this interpretation of the behaviour of observed abundance ratios such as [α/Fe] versus [Fe/H] in different galactic systems is known as the time-delay model (Tinsley 1979; Matteucci & Greggio 1986; Matteucci 2012). Other elements such as Al are also released in SNII explosions. The production of Al depends on C and N and increases with metallicity until SNIa sets in and the [Al/Fe] decreases. This makes [Al/Fe] another good tracer for what kind of galaxy a star was formed in (Hawkins et al. 2015; Das, Hawkins & Jofré 2020; Buder et al. 2022). Apart from iron, Mn is also mainly produced in SNIa and the relation between [Mg/Mn] and [Al/Fe] provides a further diagnostic to distinguish between stars born in galaxies of different mass [for a more detailed description of this, see for example Das et al. (2020) and Buder et al. (2022) and references therein]. Because the dwarf galaxies and the Milky Way are very different in mass (e.g. ratio $\sim$1:4 or $M_{\rm GES} \sim 10^{10} M_\odot$ for GES ; Belokurov et al. 2018; Helmi et al. 2018; Feuillet et al. 2020; Naidu et al. 2020), the difference in the chemical abundance of the stars can be used to identify the stars originating from another galaxy than the Milky Way.

When the *ex situ* stars have been identified, the next step is to determine their ages. Low-to-intermediate-mass-evolved red giant (RG) stars are particularly suited for this purpose because they are bright and thus can be seen at large distances and most importantly, they exhibit solar-like oscillations and hence can be studied using asteroseismology (Aerts, Christensen-Dalsgaard & Kurtz 2010, and references therein). These oscillation patterns change depending on the size and density of the stars, which makes it possible to pin down the stellar properties to an extraordinary precision (more on this in Section 4). With an asteroseismic analysis, it is possible to determine the stellar age to better than 25 per cent (Casagrande, Aguirre & Serenelli 2016; Silva Aguirre et al. 2018). The ages of the stars can be used to estimate when the merger happened because we may assume that all star formation took place in the galaxy before it was fully disrupted, and also because during mergers gas is stripped off, removing the galaxy from the fuel to produce stars.

As we mainly focus on GES in this work, we briefly introduce some studies on this galaxy. The time of the GES merger has been debated since its discovery but studies using isochrone fitting or galaxy modelling have shown that the merger ended some 8–10 Gyr ago (e.g. Belokurov et al. 2018; Helmi et al. 2018; Gallart et al. 2019; Grunblatt et al. 2021). The merger time can be estimated from isochrone fitting based on the assumption that the youngest stars are formed shortly before full disruption of their parent galaxy. There are several additional interesting works worth mentioning in the context of the Galactic archaeology of the GES merger. One is the study of ν Indi by Chaplin et al. (2020). ν Indi is a metal-poor subgiant star, which they show was born *in situ* but was kinematically heated by the merger of GES. Its age has been determined to be 11.0 $\pm$ 0.7 (stat) $\pm$ 0.8 (sys) Gyr indicating that the merger must have happened 11.6 Gyr ago at the earliest. Although this is one of the best age determinations of a metal-poor star that we have, the fact that it is a single *in situ* star limits the information it can provide for the merger time. Kruijssen et al. (2020) found globular clusters expected to belong to GES and used a Neural Network trained on cosmological simulations to estimate an accretion time of 9.1 $\pm$ 0.7 Gyr ago. Although globular clusters are very useful for age determination, asteroseismology provides us with additional information and a direct measurement for the star compared to Neural Networks. Such an asteroseismic analysis was made by Montalbán et al. (2021, hereafter M21) who found seven red giant branch stars, which they classified as belonging to GES. A comparison of stellar ages and selection criteria between our work and theirs is presented in Section 5.2.1. Grunblatt et al. (2021) also determined the age of three red giant stars associated with GES and with asteroseismology

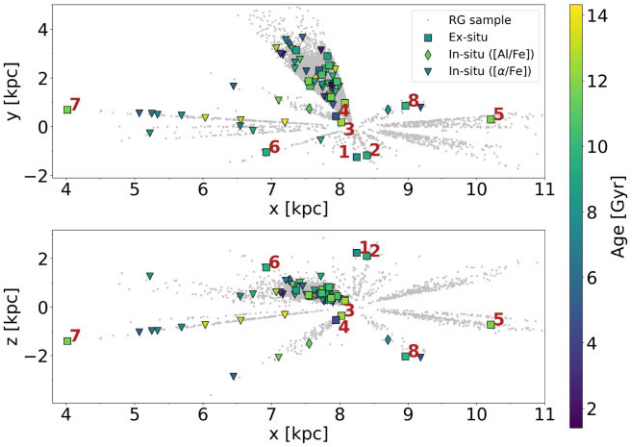

Figure 1. Position of the stellar sample in Galactocentric Cartesian coordinates. Grey dots are the full red giant star sample while the coloured points mark the stars of interest in this work, coloured by their stellar age. The different symbols denote different selection criteria (for more information, see Section 3) with the squares being the *ex situ* stars. Indices correspond to those in Table A1 but are only added to the *ex situ* from the *K2* mission in the interest of clarity.

from the *TESS* mission. They calculated a population age of GES to be $8.0^{+3.2}_{-2.3}$ Gyr.

In this paper, we explore the dynamics and chemical properties of red giant stars in order to identify which of them originates from other galaxies than the Milky Way. In Section 2, we provide an overview of our sample. In Section 3, we demonstrate how we select the sample of *ex situ* stars. For these stars, we use the Bayesian statistics software BASTA to determine their age given asteroseismic parameters, all of which is further described in Section 4. The results and a discussion on the ages and the origin of the *ex situ* stars are presented in Section 5 and a conclusion is given in Section 6.

2 DATA SAMPLE

Our full sample of stars consists of nearly 10 000 red giant stars observed by the *Kepler Space Telescope* (the original *Kepler* mission and/or the succeeding *K2* mission; Borucki et al. 2010; Koch et al. 2010; Howell et al. 2014; Stello et al. 2017) and is compiled from the red giant stars from Yu et al. (2018) (*Kepler*) and the stars from Stello et al. (2017) (K2 campaign 1) and Zinn et al. (2022) (K2 campaigns other than 1). The galactic positions of the stars in our sample can be seen in Fig. 1. This catalogue of red giant stars is cross-matched with data from *Gaia* DR2 and early Data Release 3 (eDR3; Gaia Collaboration 2016, 2018, 2021), Apache Point Observatory Galactic Evolution Experiment's DR16 (APOGEE ; Majewski et al. 2017; Ahumada et al. 2020), and the Two Micron All Sky Survey (2MASS; Skrutskie et al. 2006).

Our sample was pruned by selecting stars for which we have asteroseismic parameters ($\nu_{\rm max}$ and $\Delta\nu$, see Section 4.1), 5D phase space parameters from *Gaia* eDR3 and radial velocities from *Gaia* DR2, metallicity and temperature from APOGEE, and photometry from three filters (J, H, and K_s) from 2MASS. Furthermore, we only kept stars with `phot-bp-rb-excess-factor` $\leq$ 1.27 and a `RUWE` $<$ 1.4 to limit the stars with poor photometric and astrometric data. The 2MASS quality must be `AAA` and for APOGEE data we use stars without bad flags in `MG_FE_FLAG`, `SI_FE_FLAG`, `FE_H_FLAG`, `BAD_PIXELS`, `VERY_BRIGHT_NEIGHBOR`, `LOW_SNR`, and `SUSPECT_RV_COMBINATION` as well as `TEFF_BAD`, `METALS_BAD`, `STAR_WARN`, `VSINI_BAD`, and `STAR_BAD`. Due to the limits of our model grid, stars with $\Delta\nu$ <0.8 are also trimmed from our sample.

It has been shown that the *Gaia* parallaxes have a systematic off-set (Lindegren et al. 2021). This has been corrected for in accordance with the jupyter-notebook provided on the *Gaia* website,[1] which applies individual parallax corrections to each star. To account for potential underestimated uncertainties of APOGEE metallicities, we use a lower limit of 0.1 dex in [Fe/H] and [α/Fe] based on the discussion in Silva Aguirre et al. (2018). The orbital kinematics of the stars are calculated using GALPY[2] fast orbit estimation algorithm (Bovy 2015; Mackereth & Bovy 2018) and the `McMillan2017` potential (McMillan 2017) assuming $(U, V, W) = (11.1, 12.24, 7.25)$ km s^{-1} (Schönrich, Binney & Dehnen 2010), $v_{\rm LSR} = 221$ km s^{-1} for the local standard of rest and the Sun's distance to the galactic centre of 8.2 kpc (McMillan 2017). The uncertainties on the dynamical quantities were calculated using a bootstrap method by randomly drawing a sample of phase-space quantities based on the uncertainties and covariance matrix provided for the *Gaia* parameters. Each quantity is drawn 10 000 times and from these, the median and 16th and 84th quantiles were calculated and used as the value and corresponding uncertainty.

Table 1. Selection criteria for *ex situ* star classification.

	This work	M21
1.	L_z <0.65 × 10^3 kpc km s^{-1}	$e > 0.7$
2.	$[\alpha/\mathrm{Fe}] < -0.55\,[\mathrm{Fe/H}] - 0.25$	$[\mathrm{Mg/Fe}] < -0.2\,[\mathrm{Fe/H}] + 0.05$
3.	$[\mathrm{Mg/Mn}] > 1.8\,[\mathrm{Al/Fe}] + 0.35$	
	$[\mathrm{Mg/Mn}] > 0.25$	

3 SELECTING *EX SITU* STARS

Distinguishing *ex situ* stars from *in situ* stars is not a trivial process. The sample might be contaminated by *in situ* stars that were, for example, heated by mergers and some *ex situ* stars might have orbits that are not distinguishable from the *in situ* stars. There is also a possibility of contamination of *in situ* stars due to for example, ill-determined observed properties, or underestimated uncertainties. To combat this and get as pure a sample of *ex situ* stars as possible, we make a stringent selection. This robust selection is based on a cut in dynamical space and two cuts in different chemical spaces (see Table 1). As mentioned in Section 1, the Milky Way has merged with several galaxies in the past, meaning it is possible that the *ex situ* stars we find are not all from the same merger remnant (see Section 5.2). We, therefore, distinguish between *ex situ* and GES stars throughout this work.

The first selection criterion is in dynamic space meaning in energy (E) and angular momentum (L_z). This has become a common method of identifying *ex situ* and GES stars and was partly also how the GES stars were discovered in Helmi et al. (2018). In their work, they used a limit of L_z <0.15e3 kpc km s^{-1} to find the GES stars but to be more conservative we select stars with angular momentum L_z <0.65e3 kpc km s^{-1}. Negative angular momentum means that the stars are counter-rotating compared to the rest of the Milky Way stars that have positive angular momenta and thus it is an indication that these stars are not formed *in situ*. In Fig. 2, the full red giant star sample is in grey dots and the stars from this dynamic selection are

[1] https://www.cosmos.esa.int/web/gaia/edr3-code
[2] http://github.com/jobovy/galpy

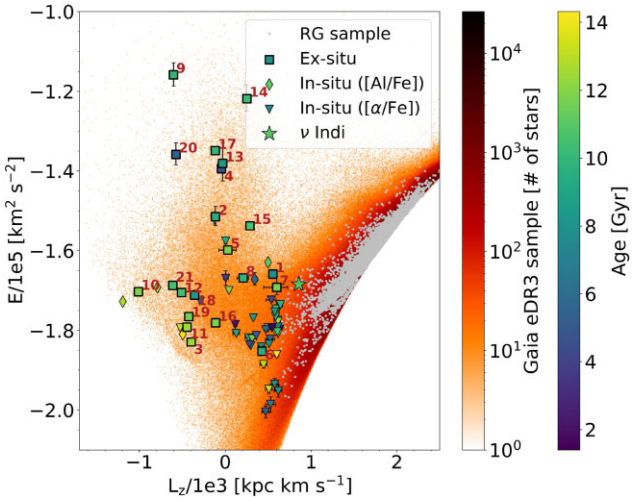

Figure 2. Distribution of stars in L_z –E space. The grey points denote the full sample of RG stars, the different symbols denote the classification of our selected stars as described in Section 3, and the orange background stars are the full *Gaia* eDR3 sample. The star symbol is ν Indi with age from Chaplin et al. (2020). All *ex situ* stars are marked with the indices corresponding to those in Table A1.

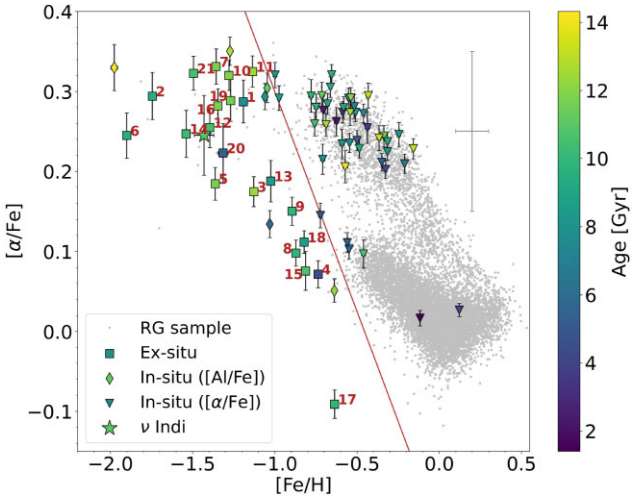

Figure 3. [α/Fe] versus metallicity abundance. Markers, colours, and indices are the same as in Fig. 2. The red line marks our selection criterion (see Table 1) and the error bar in the top corner represents 0.1 dex error on both axis. The metallicity for ν Indi is from Chaplin et al. (2020).

marked by coloured symbols. The full sample of *Gaia* eDR 3 stars (with RUWE < 1.4) are shown in orange shade for easier comparison to other works. The selection leaves us with 70 stars and we determine the ages for all of them.

The dynamics cut is not sufficient to fully exclude the *in situ* stars. Therefore, we make two additional cuts in chemical space (see Table 1). The first is in [α/Fe] versus [Fe/H] space, as shown in Fig. 3. Here, [α/Fe] is defined as $\frac{1}{2}$([Mg/Fe] + [Si/Fe]) following Salaris et al. (2018). In this plot, there are two distinct populations, one that correlates with the *in situ* stars at high [Fe/H] abundance and one at lower [Fe/H], which matches with our expectations of them being *ex situ* stars. We make a division between these two populations with a line at [α/Fe] > -0.55[Fe/H] $- 0.25$ (red line in Fig. 3). All stars from the dynamical selection that fall above this criteria are

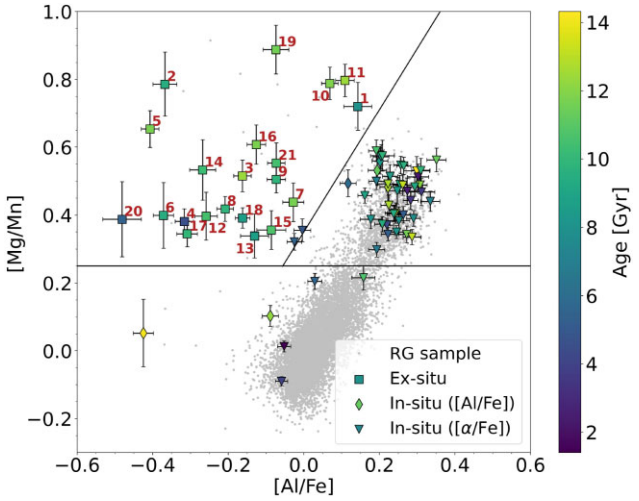

Figure 4. [Mg/Mn] versus [Al/Fe] abundance with lines from Horta et al. (2021) (see also Table 1). Markers, colours, and indices are the same as in Fig. 2.

marked with triangles and are denoted as *in situ* stars. With this cut, we sort out 43 of the 70 stars and classify them as *in situ* stars.

Lastly, a cut is made in [Mg/Mn] versus [Al/Fe] space based on the chemical evolution of galaxies described in Section 1. The lines dividing the populations are based on Horta et al. (2021) (see Fig. 4 and Table 1). Here, stars in the upper left corner are regarded as *ex situ* stars. Stars that are removed from the *ex situ* sample due to this cut are marked with diamonds unless they were already removed due to the [α/Fe] selection, in which case they remain denoted with triangles. This last cut removes six additional stars and deem them *in situ* stars.

Based on the above-mentioned criteria, we also calculated the membership probability of the stars. This is done with a bootstrap method by randomly drawing the chemical abundances from a Gaussian distribution based on the mean and uncertainties of each element. The probability is calculated with both the APOGEE given uncertainties and with uncertainties of 0.1 dex on [Fe/H] and [α/Fe] based on the argument in Section 2. For each star, the abundances where drawn 10 000 times and for each combination the classification as *ex situ* or *in situ* is determined. The probability of the stars being *ex situ* stars is given in Table A2. Based on the probabilities, one star that appears to be within both chemical selection criteria actually only has a 31 per cent (43 per cent) probability of being an *ex situ* star with 0.1 dex (APOGEE given) uncertainties on [Fe/H] and [α/Fe]. We therefore classify it as *in situ* and denote it with a triangle. Stars with probability > 50 per cent are classified as *ex situ* stars and marked with squares.

We find a total of 21 likely *ex situ* stars in our sample. These stars are marked with indices in all figures for easier identification. The relation between indices and KIC and EPIC ID's can be seen in Table A1. We note that of the 70 stars purely selected in dynamical space only $\sim$1/3 are classified as *ex situ* stars. This shows that a simple selection in L_z can result in significant amounts of contamination.

In Fig. 5, we show the stars in a number of different chemical spaces. Common for all is that the stars we select as *ex situ* appear to be a different population than the grey points we expect to be *in situ* stars. This strengthens our assumption that these stars indeed are formed in different galaxies.

Six of the classified *in situ* stars are on retrograde orbits ($L_z < 0$ kpc km s^{-1} in Fig. 2), which is peculiar for *in situ* stars. They are

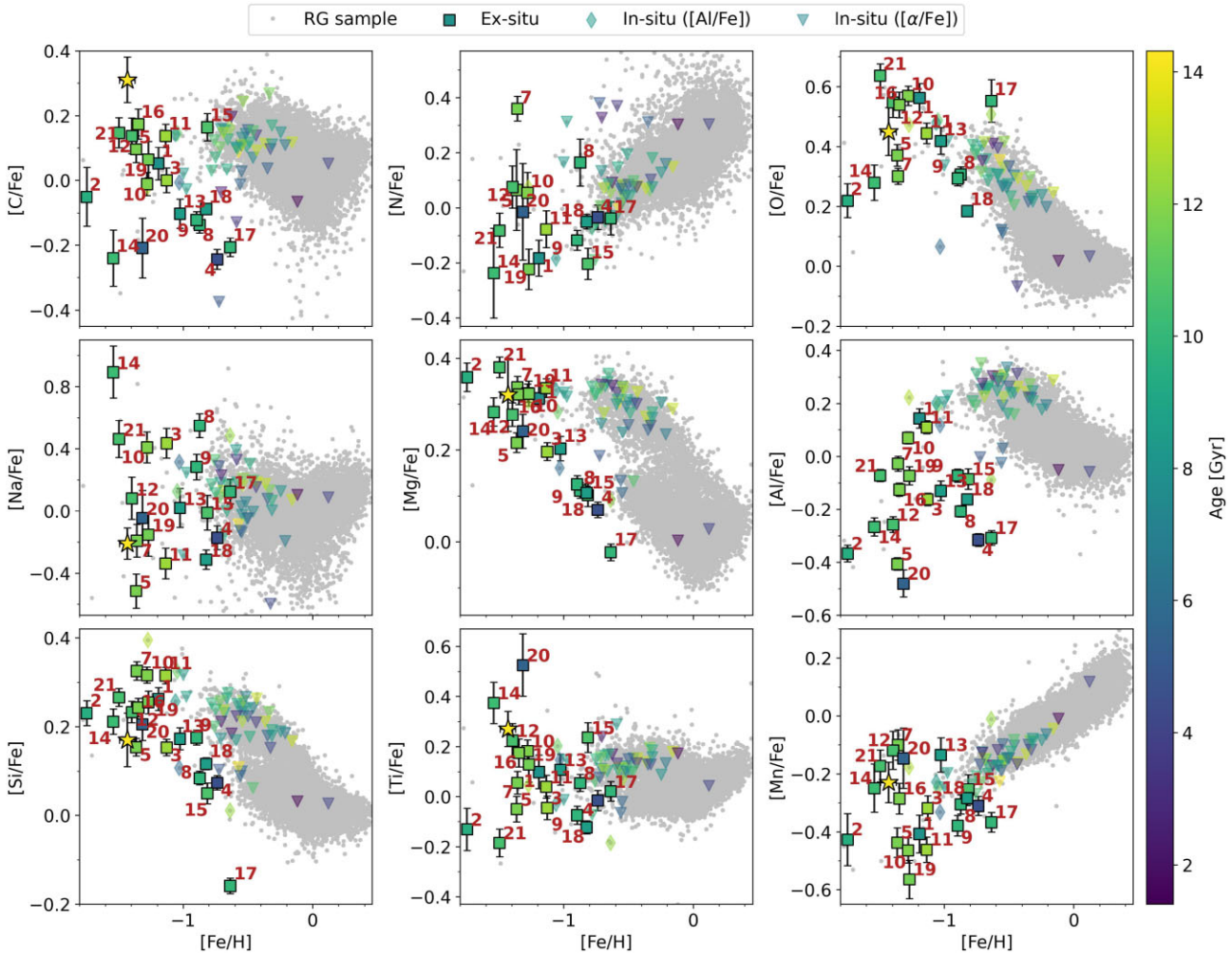

Figure 5. Different metallicities for our sample of red giant stars. Not all abundances were available for the all stars. The colour and indices are the same as previous figures. All figures have [Fe/H] in the *x*-axis with the same scale.

removed from the *ex situ* sample based on chemistry but a follow-up spectroscopic survey of these stars could clarify their classifications. In this work, we keep them as *in situ* and note it is stars #42, 44, 55, 58, 68, and 70 in Fig. A3, and Tables A1 and A2.

4 AGE DETERMINATION

4.1 Asteroseismology

As mentioned in Section 1, we use constraints from asteroseismology to determine the stellar ages of our sample. Asteroseismology is the study of how the stars oscillate and vibrate. The great advantage of asteroseismology is that the pattern in the power spectrum of the photometric time series is structurally identical for all solar-like stars. The power spectrum pattern consists of frequencies (ν) that have a very regular comb structure (at least for slowly rotating stars) and follows a Gaussian-like shape in power as a function of frequency (see e.g. Aerts et al. 2010; Basu 2016). As solar-like oscillators show this general structure, we can decompose this pattern into two global asteroseismic parameters: the large frequency separation ($\Delta\nu$) and the frequency at maximum power ($\nu_{\rm max}$). As the name suggests, $\nu_{\rm max}$ is the frequency where the Gaussian-like distribution peaks and the large frequency separation ($\Delta\nu$) is the difference in frequency between oscillations of the same angular degrees (l) but of consecutive radial order (n) hence

$$\Delta\nu_l(n) = \nu_{n,l} - \nu_{n-1,l}. \tag{1}$$

Ulrich (1986) and Christensen-Dalsgaard (1988) have analytically shown that $\Delta\nu$ scales with radius (R) and mass (M) of the star in the following manner:

$$\frac{\Delta\nu}{\Delta\nu_\odot} \simeq \left(\frac{M}{\rm M_\odot}\right)^{1/2}\left(\frac{R}{\rm R_\odot}\right)^{-3/2}. \tag{2}$$

Furthermore, Brown et al. (1991), Kjeldsen & Bedding (1995), and Bedding & Kjeldsen (2003) found a semi-empirical scaling relation based on the frequency of maximum power, which scale with mass, radius, and effective surface temperature ($T_{\rm eff}$) of the star

$$\frac{\nu_{\rm max}}{\nu_{\rm max,\odot}} \simeq \left(\frac{M}{\rm M_\odot}\right)\left(\frac{R}{\rm R_\odot}\right)^{-2}\left(\frac{T_{\rm eff}}{\rm T_{eff,\odot}}\right)^{-1/2}. \tag{3}$$

Combining equations (2) and (3), we can estimate the mass and radius of the star only based on the asteroseismic parameters and the surface temperature. The mass and radius are determined as

$$\left(\frac{M}{\rm M_\odot}\right) \simeq \left(\frac{\nu_{\rm max}}{\nu_{\rm max,\odot}}\right)^{3}\left(\frac{\Delta\nu}{\Delta\nu_\odot}\right)^{-4}\left(\frac{T_{\rm eff}}{\rm T_{eff,\odot}}\right)^{3/2} \tag{4}$$

and

$$\left(\frac{R}{R_\odot}\right) \simeq \left(\frac{\nu_{\rm max}}{\nu_{\rm max,\odot}}\right)\left(\frac{\Delta\nu}{\Delta\nu_\odot}\right)^{-2}\left(\frac{T_{\rm eff}}{T_{\rm eff,\odot}}\right)^{1/2}. \quad (5)$$

This way the asteroseismic parameters are directly related to the physical properties of the star. The scaling relations between the observables $\Delta\nu$ and $\nu_{\rm max}$ (along with $T_{\rm eff}$) and the stellar properties like the mass and radius of the star are one of the great successes of asteroseismology. Asteroseismology narrows down the likely parameter space and provides tight constraints valuable for age determination.

The resolution of the power spectra depends on, for example, the length of time series data, and if the resolution is good enough individual mode frequencies can be extracted. This is especially the case for many *Kepler* stars. Individual frequencies can greatly improve the precision of the fits because they can constrain the stellar properties even further than $\Delta\nu$ and $\nu_{\rm max}$.

For extraction and identification of the frequencies, we use the python package PBJAM (Nielsen et al. 2021). An example of a fit to the power spectrum from the peak-bagging is shown in Fig. A1 and examples of the echelle diagrams are shown in Fig. A2. A table with all extracted frequencies is available in the online material. Although both $l = 0$ and $l = 2$ modes are acquired by PBJAM, the grid only contains $l = 0$ modes and only these were fitted. The frequencies have been corrected for the Doppler shift caused by the stellar line-of-sight movement in accordance with Davies et al. (2014). If individual modes are not available, we use the $\nu_{\rm max}$ and $\Delta\nu$ values from the SYD pipeline (Huber et al. 2009) and an AI-detector for the classification of the evolutionary state (Hon, Stello & Yu 2018; Yu et al. 2018; Zinn et al. 2020). For many of the *K2* stars an AI-vetter was used to determine the quality of the $\Delta\nu$ measurements (Reyes et al. 2022). This algorithm provides a metric for the relation of the purity and completeness and we only accept stars with this number larger than 0.6, which corresponds to a purity of ∼97 per cent and a completeness of ∼93 per cent. To account for systematic uncertainties of the *K2* stars, we added a percentage of $\Delta\nu$ and $\nu_{\rm max}$ to the uncertainties based on the standard deviation of the correction factors of different pipelines in Zinn et al. (2022, their table 3). We estimated the systematic $\nu_{\rm max}$ uncertainty to be 0.3 per cent for stars that are known to be in the red giant branch (RGB) phase and 0.7 per cent for those in the red clump (RC) (or unknown) phase. The systematic $\Delta\nu$ uncertainty is estimated to be 0.3 per cent for RGB and 0.4 per cent for RC (or unknown) phase.

For the stars that only had $\Delta\nu$ and $\nu_{\rm max}$, we made a consistency check with the APOKASC sample (Pinsonneault et al. 2018) and the K2 GAP DR3 sample (Zinn et al. 2022) for the *Kepler* and *K2* stars, respectively. All stars in this work that were available in one of the two studies had consistent $\Delta\nu$ and $\nu_{\rm max}$ values within $\pm1\sigma$ of the respective studies, except star #5. It appears the SYD pipeline overestimates the $\nu_{\rm max}$ of this star with ∼2 μHz compared to other pipelines. When computing the stellar properties for star #5 with the K2 GAP DR3, $\nu_{\rm max}$ also resulted in a more consistent fit with respect to the other input parameters and we chose to use this value of $\nu_{\rm max}$ for this star. For all other stars, we keep the values from the SYD pipeline.

4.2 BASTA

To determine the stellar parameters, we use the BAyesian STellar Algorithm (BASTA; Silva Aguirre et al. 2015, 2017; Aguirre Børsen-Koch et al. 2022). The algorithm uses a pre-calculated grid of stellar tracks and Bayesian statistics to find the best-fitting stellar parameters for each star. BASTA allows for prior probability distributions to be taking into account when calculating the fits. We use the Salpeter initial mass function (Salpeter 1955) to account for the expected mass distribution of stars, favouring low-mass stars as the most abundant. For the frequency fitting, we use the two-term surface correction described in Ball & Gizon (2014). Additionally, we include an upper limit on the stellar ages of 15 Gyr. This is done to avoid non-physical solutions for stars older than the age of the Universe. Despite the solutions not being physical at above the age of the Universe (13.7 Gyr), they can still hold statistical significance and we do, therefore, not truncate the solutions at 13.7 Gyr but allow them to stretch to 15 Gyr. For the remaining parameters, we use uniform priors.

4.3 The grid

As mentioned above, BASTA uses a grid of stellar models to fit the stars. We build a quasi-random sampled (sobol; Sobol 1967) grid with ∼8000 evolutionary tracks of stellar models using the Garching Stellar Evolution Code (GARSTEC; Weiss & Schlattl 2008). The mass range of the grid is between 0.7 and 2.0 $M_\odot$, the initial metallicity $[Fe/H]_{\rm ini}$ varies between −2.4 and 0.1 dex, the α-enhancement ranged from −0.2 to 0.6 dex in steps of 0.1 dex. The mass-loss (η) ranges from 0.0 to 0.3 following the Reimers (1977) formalism. Convection in the models are parametrized using mixing-length theory (Böhm-Vitense 1958) and the mixing-length parameter is kept constant at the solar-calibrated value of 1.789 as determined from a standard solar model calibration to the Asplund et al. (2009) abundances. The primordial helium is assumed to be 0.248 (Fields et al. 2020) and the helium-to-metal ratio is $\Delta Y/\Delta Z = 1.4$. The stellar models are evolved from pre-main sequence to the beginning of the RGB, where after the models are saved and frequencies computed along the RGB, through the helium ignition and the RC and all the way to the asymptotic giant branch (AGB). This provides us with a very fine grid of stellar models in the RGB and RC phase. For all models, the radial oscillation modes ($l = 0$) are computed using the Aarhus adiabatic oscillation package (ADIPLS; Christensen-Dalsgaard 2008).

4.4 Fits

To determine the ages of the stars, we use the observed parameters [α/Fe], [Fe/H], $T_{\rm eff}$, asteroseismic values (individual frequencies with $l = 0$ or $\Delta\nu$ and $\nu_{\rm max}$, as well as evolutionary phase when available), parallax, and photometry. We use the parallax and three photometric filters (2MASS filters J, H, and K_s) to estimate the absolute magnitude of the star, which can be used as an additional constraint on the stellar properties. For this, we use the bolometric correction given by Hidalgo et al. (2018) as well as the dust map from Green et al. (2019) for computing the extinction. With the absolute magnitude, we can also get a measure for the distance to the star. These parameters are mapped to our grid of stellar models to find the best match.

When we fit the stars, different constraints can point towards slightly different solutions. Especially, the constraint of the parallax and the photometric colours can be in tension with the asteroseismic solutions. This is typically due to inaccurate or incorrect determination of one or more of the parameters, underestimates of the uncertainties, or models inaccuracies. As a test of robustness, we fitted the stars in three different ways: (i) by fitting all the parameters mentioned above, (ii) by fitting everything excluding the distance

(parallax and photometric filters), and (iii) by fitting everything excluding the asteroseismic values. Since the asteroseismic values and distance both give a direct measure of the radius of the stars (see equation 5), we compare the solution for the radius of the three fitting methods. In the cases where the calculated median radius of the fit with all parameters (i) agrees within $\pm 1\sigma$ with the solution of both other fits (ii and iii), we accept the solution (i) as robust and it is chosen because adding additional information improves the uncertainties of the solution. This check is in addition to a manual inspection of the probability distributions, to ensure the solution, for example, does not interfere with the edge of the grid.

For some stars, the three fits did not match up and gave two or even three different solutions. The fit with all the parameters (i) would then artificially be located between the two solutions of (ii) and (iii) or pushed to the edge of the two. In these cases, we will chose to trust case (ii), that is the fits including asteroseismic constraints but excluding the constraints from photometry and astrometry. We choose the asteroseismic solution as many aspects can influence the distance fit such as poorly determined parallax, colours, or dust map to name some. Only one of these parameters needs to be inaccurate for the fit to also be inaccurate, whereas the asteroseismic solution only relies on the measurement of the frequencies. In cases with tension, this makes the asteroseismic solution more reliable. Choosing the asteroseismic solution over the full fit mainly affects the uncertainties of the ages and it does not affect the conclusions drawn in this work.

Because our selection of the stars is based on E and L_z (which is calculated with the parallax), we check that the selection is not affected if we adopted the distance output form BASTA in the selection (by recalculating E and Lz). While some of the stars did move slightly in E and L_z space, they were all still part of our selection. In Table A1, we note which stars have been fitted with what method and whether we used individual frequencies or $\Delta\nu$ and $\nu_{\rm max}$. 13 of the 21 *ex situ* stars and 32 of the 49 *in situ* stars have been fitted with the distance.

The determined ages of the stars are shown as colour coding in Figs 1–5, the ages of the *ex situ* stars with uncertainties are shown in Fig. 6 and for all 70 stars in Fig. A3 and Table A1.

5 RESULTS AND DISCUSSION

5.1 Peculiar stars

A peculiar case among the *ex situ* stars is star #20, which is very young compared to the rest of the *ex situ* stars (see Fig. 6 or Table A1). Although it is likely a GES star (see Section 5.2.1), it appears too young because GES does not have any recent star formation. This is the *Kepler* star KIC 8694070, which has individual mode frequencies available. The solutions from the fits with all parameters and those without distance did not agree for this star (see discussion in Section 4.4), and we defaulted to using the fit without the distance in this case. The asteroseismic fit is good and we trust the solution, which could mean this is a young α-rich star. As described above, the asteroseismic parameters are used to find a mass and a radius of the stars, which can then be compared to an age with stellar evolutionary tracks to find the best correlation. If the star was part of a multistellar system where mass transfer have occurred, the current mass could exceed the initial mass of the star and make the star appear younger than its actual age. This is normally known as blue stragglers or in the case of old red giant stars as young α-rich stars (Martig et al. 2015; Zhang et al. 2021). This means that this star is likely not actually

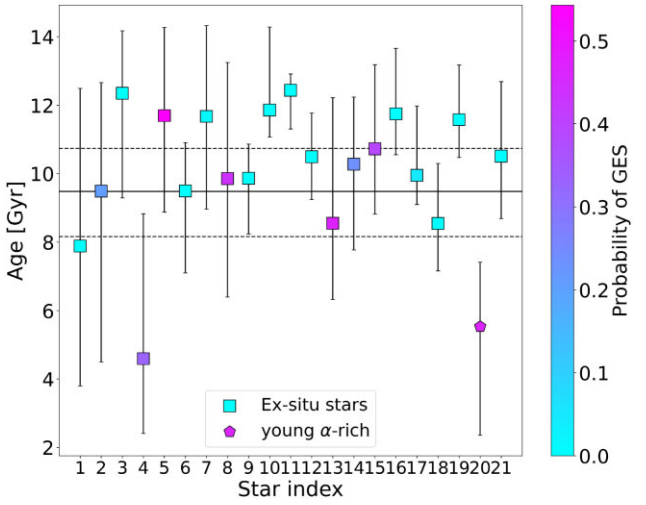

Figure 6. Ages of the *ex situ* stars with uncertainties. Indices match the ones used in other figures. Colour correlate to membership probability. The pentagon for star #20 marks that this might be a young α-rich star. The full horizontal line indicates the weighted mean age of the stars and the dashed lines indicate the standard deviation.

this young and we exclude it from any determination of mean ages in later calculations.

Star #4 have a mean age that also makes it appear young but taking the uncertainties into account it is not unrealistically young. We, therefore, keep it in our sample.

5.2 *Ex situ* stars

Through our selection criteria and membership probability calculation, we have determined which stars are *ex situ* stars in our sample. Associating them with a specific merged galaxy is more tricky. There are several studies denoting stars and globular clusters to galaxy remnants such as Massari, Koppelman & Helmi (2019), Koppelman et al. (2019), Kruijssen et al. (2020), and Naidu et al. (2020). The issue with comparison between different works are, for example, that they use different potentials to calculate the dynamics, making it hard to do direct comparison. The classification within the same potential is also not always clear and remnant stars from different galaxies overlap in both kinematic and chemical space making it nearly impossible to distinguish. In Fig. 7, we show the *ex situ* stars similar to Fig. 2 but colour coded according to eccentricity (e). It is generally accepted that GES stars have larger E than stars with similar L_z and large e but the exact boundaries are not clear. The difference in chemistry (see Fig. 8) between our *ex situ* stars suggests that these are not all of the same origin. It is possible that all these are indeed GES stars but due to the large spread in dynamics and chemistry, we have chosen to make a very conservative classification of the GES stars, which is described in Section 5.2.1.

As mentioned in Section 1, the accreted galaxies are disrupted during the merger, which quenches star formation. The mean age of the stars originating in a galaxy can therefore be interpreted as an upper limit for when the galaxy was disrupted during the merger. We present such mean values below. The mean age is calculated with a bootstrap method with 10 000 iterations.

In general, all the stars are older than 8 Gyr (except for star #20), which is in good agreement with expected ages for accreted stars (see e.g. Kruijssen et al. 2020).

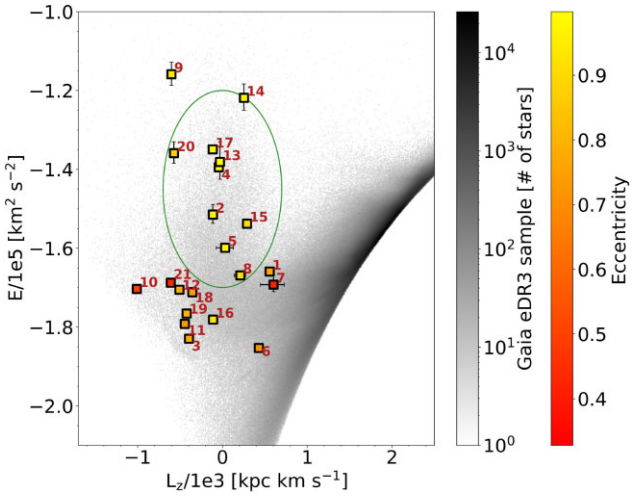

Figure 7. Similar to Fig. 2 but with only *ex situ* stars colour coded according to eccentricity of the orbits. In grey is the full sample of *Gaia* eDR3 stars. The green ellipse shows how we select the stars that are classifies as GES.

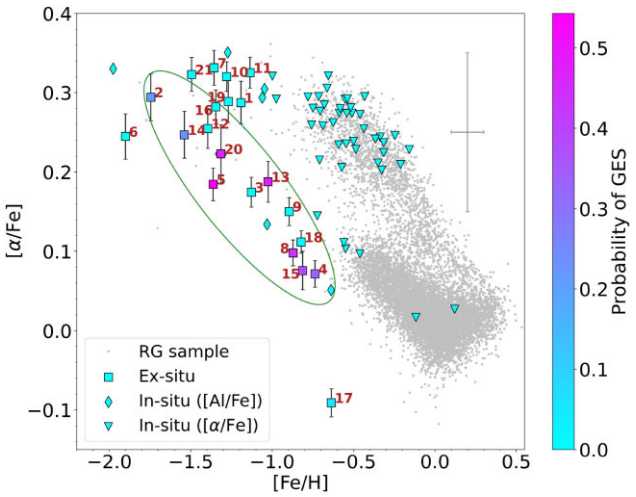

Figure 8. Similar to Fig. 3 but only *ex situ* stars coloured according to membership probability to GES. The green ellipse denotes the GES classification criterion.

5.2.1 GES

As mentioned, there is not yet a widely accepted way of determining exactly where the *ex situ* stars originate from. Our sample of *ex situ* stars can be compared directly to the sample of GES stars in Massari et al. (2019) (see their fig. 2) as they use the same potential as we do. All our stars are within the same region in E versus L_z space as their GES stars although some are very close to the edges. Naidu et al. (2020) and M21 classify GES stars based on an $e > 0.7$. This is the case for all of our *ex situ* stars apart from #7, 10, and 21. However, in Fig. 8, we expect stars from the same galaxies to follow a similar trend but there is an almost 0.2 dex difference in [α/Fe] between stars of the same [Fe/H] (stars #3, 13 and #1, 11). This could mean that the stars are not of the same origin. To be conservative, we classify stars as GES only if they have a high E and just around L_z =0 as well as a similar trend in metallicity. These stars are marked by a green ellipse in Fig. 7, and Figs 8 and A4. The ellipses are drawn with centre on (L_z, E) = (0, $-1.45e5$ km^2 s^{-2}) and radius of $0.7e3$ kpc km s^{-1} in L_z and $0.25e5$ km^2 s^{-2} in E for Fig. 7 and centred on

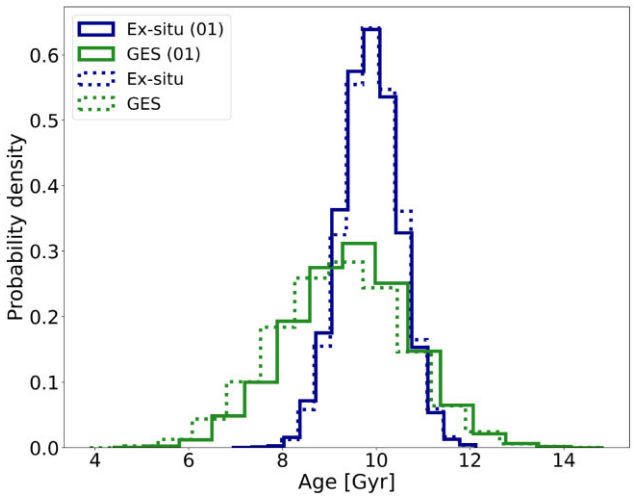

Figure 9. Age distribution of the *ex situ* population and the GES population weighted by their membership probability. Full lines (01) indicate a membership probability calculated with 0.1 dex uncertainty in [Fe/H] and [α/Fe] and dotted lines calculated with APOGEE given uncertainties.

([Fe/H],[α/Fe]) = (-1.2, 0.18), with radius 0.6 dex in [Fe/H] and 0.08 dex in [α/Fe] and tilted by $-\pi/15$ in Fig. 8. These shapes are not meant to be harsh constraints but used to emphasize where we expect the GES stars to be. The probability of the stars being members of GES is calculated based on a bootstrap method similar to the one described in Section 3. The probabilities are given in Table A2. With the provided errors from APOGEE , there is a clear separation between stars with a probability above 50 per cent and those of low probability below 4 per cent. With uncertainties of 0.1 dex for [Fe/H] and [α/Fe] is adopted, however, only one star has a probability above 50 per cent of being an GES star and the lowest of the expected GES stars has a probability of $\sim$ 20 per cent. The next probable stars is at 5 per cent marking a clear gap in this case too. If the gap is used as indicator for the classification stars #2, 4, 5, 8, 13, 14, 15, and 20 are GES stars.

Fig. 6 is colour coded according to this membership probability. We note that star #20 is part of this selection but as discussed in Section 5.1 the age of this star is likely inaccurate and it is excluded from the age calculation. The weighted mean age of our the GES stars weighted with the probability is $9.2^{1.3}_{1.4}$ Gyr with apogee uncertainties and 9.5 $\pm$ 1.3 Gyr with 0.1 dex uncertainties on the chemistry. A histogram of the weighted mean ages for the *ex situ* selection and the GES selection can be seen in Fig. 9. The main difference between the age of the different populations is the width of the distribution caused primarily by more stars contributing to the age of the *ex situ* population compared to the GES population.

The ellipses used for the selection might be a too conservative classification of GES stars. Especially, the lower E boundary in Fig. 7 could be excluding stars that appear to be GES stars in for example Fig. 8. However, the lower E region is also where *in situ* stars are potential contaminants and reducing the E boundary could lead to a less pure GES sample. We therefore chose to be conservative in our selection. As more studies on the merger galaxies are made, it is possible that more stars from our sample turn out to be GES stars. We present the ages of individual stars making it easy for later works to use the ages of the stars should improve selection criteria be determined. For reference, we note that the weighted mean age of the full *ex situ* sample (weighted with membership probability with

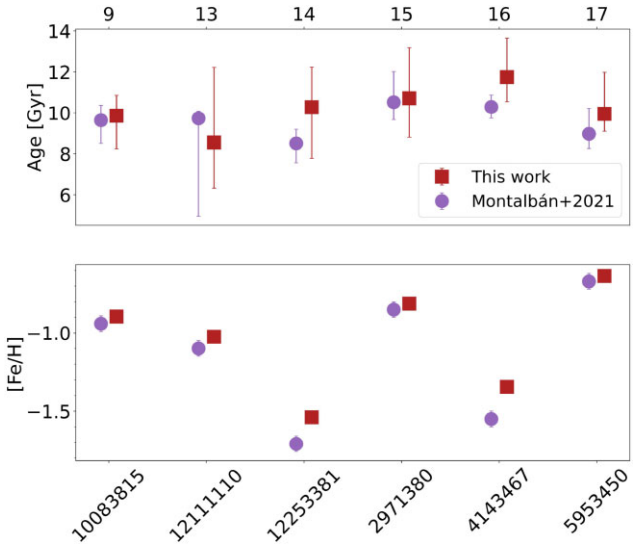

Figure 10. Comparison between our results and those of the same stars from M21. Top: ages. Bottom: iron abundance. While M21 uses APOGEE DR14, we use DR16. All stars are *Kepler* stars with KIC ID's on x-axis of bottom panel and indexes matching our figures on top for cross identification with the other figures presented in this work.

0.1 dex uncertainty and excluding #20) is 9.9 ± 0.6 Gyr and the mean age of the stars with $e > 0.7$ is 10.0 ± 0.7 Gyr.

M21 did a similar study to ours but used only RGB *Kepler* stars, different selections (see Table 1), and a different code to calculate the ages. They further used *Gaia* DR2 (Gaia Collaboration 2018) and APOGEE DR14 (Majewski et al. 2017) where we use eDR3 and DR16, respectively. In our *ex situ* sample, we find the same stars as they do except for KIC 8869235 because this was pruned in our selection due to a bad flag in STAR_WARN implying issues with the APOGEE data. The comparison between our ages and the ages presented by M21 is shown in Fig. 10. The ages agree well between the two studies and differences can be attributed to slightly different metallicities, and different software and models. Although we get similar ages for the stars we do not classify the same stars as GES but we do classify them as *ex situ*. From the sample selected by M21 we do not classify star #9, 16 and 17 as GES. On the other hand, as mentioned above, if we were to use the criteria proposed by M21 all our *ex situ* stars except #1, 7, 11, 16, 19, and 21 would be GES stars as well as our *in situ* stars #69, 75, and 76. While our selection might be too conservative, it is possible that the one presented in M21 is too broad. M21 calculated a mean age of the GES stars of 9.7 ± 0.6 Gyr and we get 9.5 ± 1.3 Gyr for our selection of GES stars. The age of our stars with M21 selection criteria is 9.2 ± 0.8 Gyr. All these ages are in agreement further enhancing the conclusion that the merger time is less than ∼10 Gyr ago.

5.2.2 *Kraken*

Another galaxy some of the stars could belong to is Kraken (Kruijssen et al. 2019; Massari et al. 2019; Kruijssen et al. 2020). Kraken is expected to have had similar mass as GES (∼3 × 10^8 $M_\odot$) and to have merged with the nascent Milky Way before GES. These stars are located at low E and at ≲7 kpc from the galactic centre. Star #7 is the closest star in our sample to the Galactic centre at ∼4 kpc. It is, however, at higher E than we expect the Kraken stars to be based on the globular clusters from Massari et al. (2019). It might, therefore, originate from somewhere else. Stars #3, 6, and 11 are closer to the expected E for Kraken. It is currently not clear where the boundaries of the Kraken remnants are and we can, therefore, not classify any of our stars as such with certainty. The accretion time of the Kraken was estimated to be $10.9^{+0.4}_{-0.7}$ Gyr by Kruijssen et al. (2020), which agrees well with all these stars being old according to our calculations. Until we have more stars in this region or a tighter constraint on their properties compared to other *ex situ* stars, it is unknown if and how many Kraken stars there are in our sample. If we assume stars #3, 6, and 11 are Kraken stars the mean age is 11.4 ± 1.3 Gyr, which is well within the estimate made by Kruijssen et al. (2020).

6 CONCLUSION

In this paper, we examine a sample of nearly 10,000 *Kepler* and *K2* stars and we find 21 stars of *ex situ* origin. Our selection is based on angular momentum (L_z), energy (E), and the [α/Fe], [Fe/H], [Al/Fe], and [Mg/Mn] abundances making it very stringent to ensure a high likelihood of choosing only *ex situ* stars.

Using asteroseismology from *Kepler* and *K2*, 5D phase space data from *Gaia* eDR3, radial velocities from *Gaia* DR2, along with temperature and metallicity from APOGEE DR16, we derive their stellar properties using the Bayesian framework of BASTA. We present ages for all 21 *ex situ* stars as well as 49 *in situ* stars.

All the *ex situ* stars are consistent with being older than 8 Gyr (except for one that is likely a young α-rich star), which is expected because most massive mergers took place in the early Galactic history.

We make a conservative classification of the *ex situ* stars and denote eight of them to be GES stars with a mean age of 9.5 ± 1.3 Gyr, which agrees with current estimates of a merger time around 8–10 Gyr ago. We compare our stellar ages to those found be Montalbán et al. (2021) and demonstrate similar results but based on different methods. The classification of GES stars between the studies deviate but we get similar mean ages of the GES stars regardless.

The remaining 13 stars are *ex situ* stars of debatable origin and some of them could also belong to GES. It is possible that three of these stars belong to the dwarf galaxy Kraken and their mean ages are estimated to be 11.4 ± 1.3 Gyr in agreement with estimates from Kruijssen et al. (2020). It is also possible that they belong to Thamnos (Koppelman et al. 2019) or Sequoia (Myeong et al. 2019) or some other yet undefined merger event.

With more data becoming available from for example the *TESS* mission, it might be possible to find even more asteroseismic merger remnant stars in the future. With more stars with precise ages it might be possible to distinguish stars from different origins based on not only their kinematics and chemistry but also their ages.

Due to the large impact mergers have had on the Milky Way's evolution, the stars presented in this work contribute important information to better understand how the mergers happened and what impact they have had on our present-day Milky Way.

SOFTWARE

The research for this publication was coded in PYTHON (v. 3.8.5; Van Rossum & Drake 2009) and included its packages ASTROPY (v. 4.0.2; Astropy Collaboration 2013, 2018), GALPY (v. 1.6.0; Bovy 2015), MATPLOTLIB (v. 3.3.2; Hunter 2007), NUMPY (v. 1.19.2; Harris et al. 2020), VAEX (v. 3.0.0; Breddels & Veljanoski 2018), IPYTHON (v. 7.19.0; Pérez & Granger 2007), JUPYTER (v. 2.2.6; Kluyver et al. 2016), and SPYDER (v. 4.1.5; Raybaut 2009). For frequency peak bagging, we used PBJAM (Nielsen et al. 2021) and for stellar

properties determination we used BASTA (Aguirre Børsen-Koch et al. 2022) (pre-public release version).

ACKNOWLEDGEMENTS

We would like to thank the referee for carefully reviewing the manuscript and suggesting changes that have improved the quality of the paper.

The authors thank Joel Zinn for kindly providing the K2 GAP DR3 data prior to its public release. The authors thank Eduardo Balbinot for providing *E* and *Lz* values for the sample of *Gaia* eDR3 stars.

Funding for the Stellar Astrophysics Centre was provided by The Danish National Research Foundation (grant agreement no. DNRF106). AH acknowledges support from a Spinoza prize from the Netherlands Research Council (NWO). HHK gratefully acknowledges financial support from a Fellowship at the Institute for Advanced Study. AS acknowledges support from the European Research Council Consolidator Grant funding scheme (project ASTEROCHRONOMETRY, G.A. n. 772293, http://www.asterochronometry.eu). JMDK gratefully acknowledges funding from the Deutsche Forschungsgemeinschaft (DFG, German Research Foundation) through an Emmy Noether Research Group (grant number KR4801/1-1), as well as from the European Research Council (ERC) under the European Union's Horizon 2020 research and innovation programme via the ERC Starting Grant MUSTANG (grant agreement number 714907). CL acknowledges funding from the European Research Council (ERC) under the European Union's Horizon 2020 research and innovation programme (grant agreement number 852839). JY acknowledges partial support from ERC Synergy Grant WHOLE SUN 810218.

This work has made use of data from the European Space Agency (ESA) mission *Gaia* (https://www.cosmos.esa.int/gaia), processed by the *Gaia* Data Processing and Analysis Consortium (DPAC, https://www.cosmos.esa.int/web/gaia/dpac/consortium). Funding for the DPAC has been provided by national institutions, in particular the institutions participating in the *Gaia* Multilateral Agreement. This publication makes use of data products from the Two Micron All Sky Survey, which is a joint project of the University of Massachusetts and the Infrared Processing and Analysis Center/California Institute of Technology, funded by the National Aeronautics and Space Administration and the National Science Foundation.

DATA AVAILABILITY

The data underlying this article will be available in its online supplementary material upon publication.

REFERENCES

Aerts C., Christensen-Dalsgaard J., Kurtz D. W., 2010, Asteroseismology. Springer, Dordrecht
Aguirre Børsen-Koch V. et al., 2022, MNRAS, 509, 4344
Ahumada R. et al., 2020, ApJS, 249, 3
Asplund M., Grevesse N., Sauval A. J., Scott P., 2009, ARA&A, 47, 481
Astropy Collaboration, 2013, A&A, 558, A33
Astropy Collaboration, 2018, AJ, 156, 123
Ball W. H., Gizon L., 2014, A&A, 568, A123
Basu S., 2016, Living Rev. Solar Phys., 13, 2
Bedding T. R., Kjeldsen H., 2003, PASA, 20, 203
Bell E. F. et al., 2008, ApJ, 680, 295
Belokurov V., Erkal D., Evans N. W., Koposov S. E., Deason A. J., 2018, MNRAS, 478, 611
Böhm-Vitense E., 1958, Z. Astrophys., 46, 108
Borucki W. J. et al., 2010, Science, 327, 977
Bovy J., 2015, ApJS, 216, 29
Breddels M. A., Veljanoski J., 2018, A&A, 618, A13
Brown T. M., Gilliland R. L., Noyes R. W., Ramsey L. W., 1991, ApJ, 368, 599
Buder S. et al., 2022, MNRAS, 510, 2407
Casagrande L., Aguirre V. S., Serenelli A. M., 2016, IAU Focus Meeting, 29B, 680
Chaplin W. J. et al., 2020, Nat. Astron., 4, 382
Christensen-Dalsgaard J., 1988, in Christensen-Dalsgaard J., Frandsen S., eds, Proc. IAU Symp. 123, Advances in Helio- and Asteroseismology. Reidel, Dordrecht, p. 295
Christensen-Dalsgaard J., 2008, Ap&SS, 316, 113
Das P., Hawkins K., Jofré P., 2020, MNRAS, 493, 5195
Davé R., 2008, MNRAS, 385, 147
Davies G. R., Handberg R., Miglio A., Campante T. L., Chaplin W. J., Elsworth Y., 2014, MNRAS, 445, L94
Elias L. M., Sales L. V., Helmi A., Hernquist L., 2020, MNRAS, 495, 29
Feuillet D. K., Feltzing S., Sahlholdt C. L., Casagrande L., 2020, MNRAS, 497, 109
Fields B. D., Olive K. A., Yeh T.-H., Young C., 2020, J. Cosmol. Astropart. Phys., 2020, 010
Freeman K., Bland-Hawthorn J., 2002, ARA&A, 40, 487
Gaia Collaboration, 2016, A&A, 595, A1
Gaia Collaboration, 2018, A&A, 616, A1
Gaia Collaboration, 2021, A&A, 649, A1
Gallart C., Bernard E. J., Brook C. B., Ruiz-Lara T., Cassisi S., Hill V., Monelli M., 2019, Nat. Astron., 3, 932
Green G. M., Schlafly E., Zucker C., Speagle J. S., Finkbeiner D., 2019, ApJ, 887, 93
Grunblatt S. K. et al., 2021, ApJ, 916, 88
Harris C. R. et al., 2020, Nature, 585, 357
Hawkins K., Jofré P., Masseron T., Gilmore G., 2015, MNRAS, 453, 758
Helmi A., 2020, ARA&A, 58, 205
Helmi A., White S. D. M., de Zeeuw P. T., Zhao H., 1999, Nature, 402, 53
Helmi A., Babusiaux C., Koppelman H. H., Massari D., Veljanoski J., Brown A. G. A., 2018, Nature, 563, 85
Hidalgo S. L. et al., 2018, ApJ, 856, 125
Hon M., Stello D., Yu J., 2018, MNRAS, 476, 3233
Horta D. et al., 2021, MNRAS, 500, 1385
Howell S. B. et al., 2014, PASP, 126, 398
Huber D., Stello D., Bedding T. R., Chaplin W. J., Arentoft T., Quirion P. O., Kjeldsen H., 2009, Commun. Asteroseismol., 160, 74
Hunter J. D., 2007, Comput Sci Eng., 9, 90
Iben Icko J., Tutukov A. V., 1991, ApJ, 370, 615
Jean-Baptiste I., Di Matteo P., Haywood M., Gómez A., Montuori M., Combes F., Semelin B., 2017, A&A, 604, A106
Kjeldsen H., Bedding T. R., 1995, A&A, 293, 87
Kluyver T. et al., 2016, in Loizides F., Scmidt B., eds, Positioning and Power in Academic Publishing: Players, Agents and Agendas. IOS Press, Netherlands, p. 87
Koch D. G. et al., 2010, ApJ, 713, L79
Koppelman H. H., Helmi A., Massari D., Price-Whelan A. M., Starkenburg T. K., 2019, A&A, 631, L9
Koppelman H. H., Bos R. O. Y., Helmi A., 2020, A&A, 642, L18
Kromer M. et al., 2015, MNRAS, 450, 3045
Kruijssen J. M. D., Pfeffer J. L., Reina-Campos M., Crain R. A., Bastian N., 2019, MNRAS, 486, 3180
Kruijssen J. M. D. et al., 2020, MNRAS, 498, 2472
Lindegren L. et al., 2021, A&A, 649, A4
Mackereth J. T., Bovy J., 2018, PASP, 130, 114501
Majewski S. R. et al., 2017, AJ, 154, 94
Martig M. et al., 2015, MNRAS, 451, 2230
Massari D., Koppelman H. H., Helmi A., 2019, A&A, 630, L4
Matteucci F., 2012, Chemical Evolution of Galaxies. Springer, Heidelberg
Matteucci F., Greggio L., 1986, A&A, 154, 279
McMillan P. J., 2017, MNRAS, 465, 76
Montalbán J. et al., 2021, Nat. Astron., 5, 640 (M21)

Myeong G. C., Vasiliev E., Iorio G., Evans N. W., Belokurov V., 2019, MNRAS, 488, 1235
Naidu R. P., Conroy C., Bonaca A., Johnson B. D., Ting Y.-S., Caldwell N., Zaritsky D., Cargile P. A., 2020, ApJ, 901, 48
Nielsen M. B. et al., 2021, AJ, 161, 62
Nissen P. E., Schuster W. J., 2010, A&A, 511, L10
Pérez F., Granger B. E., 2007, Comput. Sci. Eng., 9, 21
Pinsonneault M. H. et al., 2018, ApJS, 239, 32
Raybaut P., 2009, available online at pythonhosted.org
Reimers D., 1977, A&A, 57, 395
Reyes C., Stello D., Hon M., Zinn J. C., 2022, MNRAS, 511, 5578
Salaris M., Cassisi S., Schiavon R. P., Pietrinferni A., 2018, A&A, 612, A68
Salpeter E. E., 1955, ApJ, 121, 161
Schönrich R., Binney J., Dehnen W., 2010, MNRAS, 403, 1829
Silva Aguirre V. et al., 2015, MNRAS, 452, 2127
Silva Aguirre V. et al., 2017, ApJ, 835, 173
Silva Aguirre V. et al., 2018, MNRAS, 475, 5487
Skrutskie M. F. et al., 2006, AJ, 131, 1163
Sobol I. M., 1967, USSR Comp. Math. Math. Phys., 7, 4
Stello D. et al., 2017, ApJ, 835, 83
Tinsley B. M., 1979, ApJ, 229, 1046
Ulrich R. K., 1986, ApJ, 306, L37
Van Rossum G., Drake F. L., 2009, Python 3 Reference Manual. CreateSpace, Scotts Valley, CA
Villalobos Á., Helmi A., 2008, MNRAS, 391, 1806
Weiss A., Schlattl H., 2008, Ap&SS, 316, 99
Whelan J., Iben Icko J., 1973, ApJ, 186, 1007
Yu J., Huber D., Bedding T. R., Stello D., Hon M., Murphy S. J., Khanna S., 2018, ApJS, 236, 42
Zhang M. et al., 2021, ApJ, 922, 145
Zinn J. C. et al., 2020, ApJS, 251, 23
Zinn J. C. et al., 2022, ApJ, 926, 191

SUPPORTING INFORMATION

Supplementary data are available at *MNRAS* online.

PBjam_frequencies.ascii

Please note: Oxford University Press is not responsible for the content or functionality of any supporting materials supplied by the authors. Any queries (other than missing material) should be directed to the corresponding author for the article.

APPENDIX A: STARS IN OUR SAMPLE

Table A1. Table of stars from our sample. The columns contain the index of the stars used throughout the paper (INDEX), the ID of the stars where 'Kepler' denotes stars with KIC ID's and K2Cx denotes stars from the *K2* mission with *x* corresponding to the campaign number and corresponding EPIC ID. The asteroseismic parameters from PBJAM or the SYD pipeline in μHz. The following column is the distance to the Galactic centre in kpc and the eccentricity of the stars. The distance, radius, and ages with uncertainties (16th and 84th percentile from the posterior distribution) are derived from BASTA in pc, $R_\odot$, and Gyr, respectively. The last column contains information about how each star was fitted. 'Indi' denotes stars that had individual frequencies available, 'Seis' indicates stars that only had ν_{max} and $\Delta\nu$ available, and 'with(w/o) dist' denotes stars where the distance was (not) fitted.

INDEX	ID	$\Delta\nu$	ν_{max}	R_{GC}	e	Distance	R_*	Age	FIT
1	K2C1 201609020	4.01 ± 0.06	31.63 ± 0.91	8.34 ± 0.01	0.77 ± 0.02	2927^{+90}_{-71}	$10.1^{+0.8}_{-0.4}$	$7.88^{+4.61}_{-4.09}$	Indi, w/o dist
2	K2C1 201709805	3.85 ± 0.03	30.06 ± 0.86	8.48 ± 0.01	0.97 ± 0.01	3138^{+70}_{-55}	$10.4^{+0.8}_{-0.3}$	$9.49^{+3.17}_{-4.99}$	Indi, w/o dist
3	K2C3 205934106	13.12 ± 0.14	145.94 ± 4.28	8.03 ± 0.01	0.78 ± 0.01	459^{+5}_{-5}	$4.3^{+0.1}_{-0.1}$	$12.35^{+1.82}_{-3.06}$	Indi, with dist
4	K2C3 206516677	3.96 ± 0.06	30.19 ± 2.05	7.96 ± 0.01	0.99 ± 0.01	964^{+39}_{-38}	$11.0^{+0.8}_{-0.8}$	$4.59^{+4.23}_{-2.19}$	Seis, w/o dist[a]
5	K2C4 211001845	3.49 ± 0.08	27.59 ± 0.98	10.21 ± 0.08	0.98 ± 0.03	2288^{+47}_{-38}	$10.5^{+0.4}_{-0.2}$	$11.69^{+2.57}_{-2.82}$	Seis, w/o dist[b]
6	K2C6 212319585	3.68 ± 0.27	27.00 ± 1.28	7.00 ± 0.05	0.72 ± 0.03	2310^{+28}_{-28}	$10.3^{+0.2}_{-0.2}$	$9.49^{+1.41}_{-2.40}$	Indi, with dist
7	K2C7 213616808	1.23 ± 0.05	6.32 ± 1.96	4.08 ± 0.61	0.42 ± 0.15	4793^{+91}_{-87}	$21.6^{+0.8}_{-0.7}$	$11.67^{+2.65}_{-2.71}$	Seis, with dist
8	K2C8 220238966	4.07 ± 0.05	30.78 ± 2.09	9.00 ± 0.04	0.92 ± 0.03	2720^{+52}_{-48}	$9.8^{+0.4}_{-0.3}$	$9.85^{+3.40}_{-3.45}$	Seis, w/o dist
9	Kepler 10083815	2.59 ± 0.01	17.99 ± 0.38	8.15 ± 0.01	0.94 ± 0.01	2425^{+24}_{-23}	$13.0^{+0.2}_{-0.2}$	$9.86^{+1.00}_{-1.62}$	Indi, with dist
10	Kepler 10460723	3.14 ± 0.02	22.97 ± 0.45	8.07 ± 0.01	0.49 ± 0.01	2402^{+16}_{-16}	$11.1^{+0.1}_{-0.1}$	$11.86^{+2.42}_{-0.80}$	Indi, with dist[c]
11	Kepler 11563791	5.04 ± 0.03	43.03 ± 0.51	8.13 ± 0.01	0.74 ± 0.01	973^{+11}_{-8}	$8.2^{+0.1}_{-0.1}$	$12.44^{+0.47}_{-1.14}$	Indi, with dist
12	Kepler 11566038	3.95 ± 0.03	31.36 ± 0.32	8.17 ± 0.01	0.79 ± 0.01	1949^{+18}_{-20}	$9.7^{+0.1}_{-0.1}$	$10.49^{+1.28}_{-1.25}$	Indi, with dist
13	Kepler 12111110	3.75 ± 0.02	29.57 ± 0.37	8.34 ± 0.03	0.99 ± 0.01	3022^{+78}_{-73}	$10.5^{+0.3}_{-0.3}$	$8.55^{+3.67}_{-2.22}$	Indi, with dist
14	Kepler 12253381	3.03 ± 0.02	22.00 ± 0.40	8.24 ± 0.01	0.97 ± 0.01	2796^{+42}_{-41}	$11.6^{+0.3}_{-0.2}$	$10.27^{+1.96}_{-2.50}$	Indi, w/o dist
15	Kepler 2971380	7.88 ± 0.03	77.26 ± 0.70	7.75 ± 0.01	0.92 ± 0.01	1553^{+23}_{-22}	$6.2^{+0.1}_{-0.1}$	$10.72^{+2.46}_{-1.91}$	Indi, w/o dist
16	Kepler 4143467	5.63 ± 0.02	48.96 ± 0.57	7.77 ± 0.01	0.93 ± 0.01	2010^{+18}_{-13}	$7.6^{+0.1}_{-0.1}$	$11.75^{+1.91}_{-1.20}$	Indi, with dist
17	Kepler 5953450	12.69 ± 0.05	140.87 ± 0.83	7.94 ± 0.01	0.98 ± 0.01	1249^{+15}_{-15}	$4.6^{+0.0}_{-0.1}$	$9.95^{+2.03}_{-0.85}$	Indi, with dist
18	Kepler 6865157	1.57 ± 0.07	9.05 ± 0.28	8.00 ± 0.01	0.74 ± 0.01	3317^{+45}_{-45}	$19.1^{+0.5}_{-0.5}$	$8.54^{+1.75}_{-1.38}$	Seis, with dist
19	Kepler 7948268	11.45 ± 0.04	120.45 ± 0.82	7.97 ± 0.01	0.80 ± 0.01	1285^{+12}_{-15}	$4.8^{+0.1}_{-0.1}$	$11.58^{+1.60}_{-1.11}$	Indi, with dist
20	Kepler 8694070	4.63 ± 0.04	33.66 ± 0.42	8.04 ± 0.01	0.88 ± 0.01	2701^{+42}_{-41}	$9.7^{+1.1}_{-0.3}$	$5.54^{+1.88}_{-3.18}$	Indi, w/o dist
21	Kepler 9339711	2.84 ± 0.01	20.51 ± 0.31	8.03 ± 0.01	0.45 ± 0.01	2272^{+21}_{-28}	$12.1^{+0.2}_{-0.2}$	$10.51^{+2.18}_{-1.82}$	Indi, with dist
22	K2C11 204785972	3.34 ± 0.17	23.10 ± 1.69	6.55 ± 0.04	0.68 ± 0.01	2001^{+76}_{-63}	$12.1^{+1.5}_{-0.8}$	$7.34^{+4.39}_{-4.25}$	Seis, w/o dist
23	K2C17 251512185	4.73 ± 0.34	40.18 ± 0.77	7.74 ± 0.01	0.83 ± 0.03	1556^{+51}_{-42}	$9.1^{+0.8}_{-0.5}$	$9.18^{+3.92}_{-4.38}$	Seis, w/o dist
24	K2C2 204298932	1.69 ± 0.05	10.30 ± 0.30	6.73 ± 0.04	0.91 ± 0.03	1777^{+80}_{-71}	$18.3^{+1.0}_{-0.7}$	$9.24^{+3.91}_{-3.11}$	Seis, w/o dist
25	K2C2 205083494	1.21 ± 0.03	6.80 ± 0.20	5.23 ± 0.15	0.40 ± 0.03	3245^{+54}_{-57}	$22.4^{+0.7}_{-0.6}$	$8.17^{+1.80}_{-1.80}$	Seis, with dist
26	K2C3 205972576	4.08 ± 0.12	28.51 ± 6.21	7.19 ± 0.04	0.81 ± 0.03	2693^{+35}_{-37}	$10.1^{+0.3}_{-0.3}$	$11.62^{+2.30}_{-2.66}$	Seis, with dist
27	K2C3 205997746	5.71 ± 0.04	51.06 ± 0.86	7.59 ± 0.02	0.73 ± 0.02	1852^{+18}_{-19}	$7.5^{+0.1}_{-0.1}$	$11.29^{+2.10}_{-1.90}$	Indi, with dist

Table A1 – *continued*

INDEX	ID	$\Delta\nu$	$\nu_{\max}$	R_{GC}	e	Distance	R_*	Age	FIT
28	K2C3 206011766	1.22 ± 0.09	7.34 ± 0.20	6.65 ± 0.09	0.63 ± 0.04	4139^{+330}_{-163}	$23.2^{+3.1}_{-2.0}$	$5.69^{+5.44}_{-3.20}$	Seis, w/o dist
29	K2C6 212297999	2.60 ± 0.07	19.31 ± 0.34	7.00 ± 0.04	0.74 ± 0.02	2482^{+79}_{-68}	$13.8^{+1.0}_{-0.7}$	$7.69^{+4.28}_{-3.30}$	Seis, w/o dist
30	K2C7 213463719	5.79 ± 0.04	54.92 ± 1.38	6.56 ± 0.07	0.68 ± 0.03	1820^{+19}_{-23}	$7.9^{+0.2}_{-0.2}$	$13.19^{+1.40}_{-3.65}$	Indi, with dist
31	K2C7 213523425	4.76 ± 0.04	43.10 ± 1.57	6.04 ± 0.08	0.60 ± 0.03	2392^{+29}_{-32}	$8.9^{+0.2}_{-0.1}$	$13.18^{+0.71}_{-2.35}$	Indi, with dist
32	K2C7 213532050	8.76 ± 0.08	88.85 ± 4.22	7.20 ± 0.02	0.61 ± 0.02	1139^{+8}_{-7}	$5.7^{+0.1}_{-0.1}$	$14.32^{+0.56}_{-1.29}$	Indi, w/o dist
33	K2C7 213632986	1.29 ± 0.04	7.89 ± 0.27	5.36 ± 0.13	0.69 ± 0.01	3941^{+224}_{-139}	$22.4^{+2.1}_{-1.5}$	$6.98^{+5.01}_{-3.53}$	Seis, w/o dist
34	K2C7 213764390	1.38 ± 0.15	9.16 ± 0.38	5.10 ± 0.14	0.55 ± 0.03	3345^{+64}_{-59}	$21.6^{+0.8}_{-0.7}$	$5.32^{+1.66}_{-1.41}$	Seis, with dist
35	K2C7 213840500	3.07 ± 0.06	24.80 ± 0.91	5.28 ± 0.18	0.51 ± 0.04	2766^{+115}_{-86}	$12.8^{+0.9}_{-0.7}$	$6.66^{+4.10}_{-3.07}$	Seis, w/o dist
36	K2C7 213853964	4.26 ± 0.06	36.12 ± 2.93	5.71 ± 0.13	0.55 ± 0.03	2732^{+47}_{-66}	$9.7^{+0.3}_{-0.3}$	$7.81^{+3.18}_{-1.98}$	Indi, with dist
37	K2C8 220269276	6.36 ± 0.38	65.79 ± 2.53	9.22 ± 0.05	0.73 ± 0.03	2786^{+86}_{-89}	$8.3^{+0.4}_{-0.4}$	$4.33^{+2.87}_{-1.53}$	Seis, w/o dist
38	K2C8 220387868	3.87 ± 0.06	32.20 ± 1.01	8.73 ± 0.02	0.69 ± 0.03	1596^{+25}_{-23}	$10.5^{+0.3}_{-0.2}$	$8.20^{+1.70}_{-1.88}$	Indi, with dist
39	Kepler 10096113	4.22 ± 0.03	36.31 ± 0.59	8.34 ± 0.03	0.94 ± 0.01	3116^{+55}_{-62}	$11.6^{+0.4}_{-0.4}$	$2.12^{+0.59}_{-0.55}$	Indi, with dist
40	Kepler 10207078	4.57 ± 0.02	40.30 ± 0.65	8.06 ± 0.01	1.00 ± 0.01	1514^{+13}_{-16}	$9.3^{+0.1}_{-0.1}$	$9.40^{+0.66}_{-1.10}$	Indi, with dist
41	Kepler 10398120	1.59 ± 0.10	8.58 ± 0.27	8.05 ± 0.01	0.84 ± 0.01	1849^{+26}_{-24}	$19.3^{+0.5}_{-0.4}$	$8.59^{+1.35}_{-1.52}$	Seis, with dist
42	Kepler 10992126	1.33 ± 0.14	7.83 ± 0.22	8.16 ± 0.01	0.97 ± 0.01	1694^{+24}_{-25}	$21.2^{+0.5}_{-0.5}$	$8.86^{+1.49}_{-1.23}$	Seis, with dist
43	Kepler 11037292	2.40 ± 0.01	17.01 ± 0.25	8.16 ± 0.01	0.65 ± 0.01	2146^{+29}_{-29}	$13.8^{+0.2}_{-0.2}$	$9.72^{+2.25}_{-1.36}$	Indi, with dist
44	Kepler 11774651	4.60 ± 0.02	39.78 ± 0.43	8.28 ± 0.01	0.73 ± 0.01	2460^{+16}_{-15}	$9.0^{+0.1}_{-0.1}$	$13.18^{+0.71}_{-1.62}$	Indi, with dist
45	Kepler 12109442	4.11 ± 0.13	28.57 ± 0.83	8.13 ± 0.01	0.98 ± 0.01	1062^{+16}_{-16}	$10.1^{+0.3}_{-0.3}$	$12.05^{+1.76}_{-2.94}$	Seis, w/o dist
46	Kepler 12506245	2.97 ± 0.02	19.17 ± 0.69	8.26 ± 0.01	0.64 ± 0.01	2735^{+27}_{-28}	$11.9^{+0.3}_{-0.4}$	$12.75^{+0.78}_{-2.86}$	Indi, w/o dist
47	Kepler 1726211	3.76 ± 0.03	30.70 ± 0.63	7.87 ± 0.01	0.70 ± 0.01	1303^{+19}_{-20}	$11.8^{+0.2}_{-0.3}$	$3.37^{+0.63}_{-0.65}$	Indi, with dist
48	Kepler 2165615	4.15 ± 0.02	37.78 ± 0.98	7.75 ± 0.01	0.59 ± 0.02	3175^{+48}_{-42}	$11.4^{+0.3}_{-0.3}$	$2.45^{+0.67}_{-0.38}$	Indi, with dist
49	Kepler 2301577	4.27 ± 0.03	35.98 ± 0.95	7.73 ± 0.01	0.99 ± 0.01	3220^{+31}_{-25}	$10.8^{+0.2}_{-0.1}$	$3.67^{+0.74}_{-0.33}$	Indi, with dist
50	Kepler 2444790	2.90 ± 0.02	18.91 ± 0.80	7.77 ± 0.01	0.63 ± 0.01	3400^{+36}_{-26}	$12.4^{+0.2}_{-0.4}$	$12.73^{+1.52}_{-3.14}$	Indi, with dist
51	Kepler 2571323	4.65 ± 0.02	39.98 ± 0.30	7.72 ± 0.01	0.74 ± 0.01	2612^{+27}_{-34}	$8.9^{+0.1}_{-0.2}$	$9.81^{+2.87}_{-0.96}$	Indi, with dist
52	Kepler 2714397	4.19 ± 0.03	33.08 ± 0.64	7.95 ± 0.01	0.80 ± 0.01	965^{+6}_{-8}	$10.5^{+0.1}_{-0.2}$	$5.16^{+1.85}_{-0.47}$	Indi, with dist
53	Kepler 2831815	5.61 ± 0.03	52.88 ± 0.50	7.73 ± 0.01	0.70 ± 0.01	1893^{+24}_{-21}	$8.3^{+0.2}_{-0.2}$	$8.05^{+1.80}_{-0.96}$	Indi, with dist
54	Kepler 5371173	5.09 ± 0.02	45.78 ± 0.32	7.91 ± 0.01	0.66 ± 0.01	1677^{+12}_{-10}	$8.6^{+0.1}_{-0.1}$	$9.43^{+0.45}_{-1.12}$	Indi, with dist
55	Kepler 5698156	1.68 ± 0.03	9.73 ± 0.31	7.92 ± 0.01	0.33 ± 0.01	1348^{+13}_{-14}	$17.2^{+0.3}_{-0.3}$	$12.80^{+1.52}_{-2.15}$	Seis, with dist
56	Kepler 5792889	13.15 ± 0.05	150.71 ± 0.88	7.95 ± 0.01	0.62 ± 0.01	1257^{+11}_{-14}	$4.5^{+0.0}_{-0.1}$	$10.60^{+0.97}_{-1.05}$	Indi, with dist
57	Kepler 6267115	2.03 ± 0.01	13.52 ± 0.25	7.80 ± 0.01	0.83 ± 0.01	2815^{+47}_{-44}	$16.5^{+0.4}_{-0.3}$	$8.12^{+1.80}_{-1.86}$	Indi, with dist[c]
58	Kepler 7191496	2.47 ± 0.02	16.23 ± 0.24	7.90 ± 0.01	0.71 ± 0.01	2271^{+20}_{-10}	$13.1^{+0.1}_{-0.1}$	$14.07^{+0.78}_{-0.83}$	Indi, w/o dist
59	Kepler 7502070	4.00 ± 0.02	33.77 ± 0.68	7.85 ± 0.01	0.67 ± 0.01	2039^{+21}_{-21}	$10.1^{+0.1}_{-0.2}$	$9.25^{+2.68}_{-1.43}$	Indi, with dist
60	Kepler 7596219	2.69 ± 0.02	19.54 ± 0.37	7.98 ± 0.02	0.64 ± 0.01	3506^{+28}_{-34}	$12.6^{+0.2}_{-0.1}$	$11.36^{+2.03}_{-1.60}$	Indi, with dist
61	Kepler 7908109	5.84 ± 0.03	52.82 ± 0.53	8.02 ± 0.01	0.69 ± 0.01	1756^{+16}_{-22}	$7.7^{+0.1}_{-0.1}$	$9.80^{+1.50}_{-0.23}$	Indi, w/o dist
62	Kepler 7946809	1.76 ± 0.02	11.67 ± 0.43	8.04 ± 0.03	0.66 ± 0.01	4119^{+84}_{-78}	$18.3^{+0.8}_{-0.6}$	$7.04^{+2.88}_{-2.55}$	Seis, w/o dist
63	Kepler 8350894	2.00 ± 0.02	12.69 ± 0.29	8.03 ± 0.02	0.87 ± 0.01	4135^{+71}_{-82}	$16.6^{+0.5}_{-0.6}$	$5.84^{+2.38}_{-1.31}$	Seis, w/o dist
64	Kepler 8411446	3.94 ± 0.10	28.45 ± 1.02	7.91 ± 0.01	0.66 ± 0.01	3041^{+40}_{-38}	$10.3^{+0.3}_{-0.2}$	$10.71^{+2.29}_{-2.46}$	Seis, with dist
65	Kepler 8544630	7.55 ± 0.03	74.63 ± 0.51	7.93 ± 0.01	0.73 ± 0.01	1804^{+16}_{-17}	$6.6^{+0.1}_{-0.1}$	$8.32^{+1.43}_{-0.55}$	Indi, w/o dist
66	Kepler 9405480	2.74 ± 0.01	22.73 ± 0.37	8.04 ± 0.01	0.85 ± 0.01	1619^{+23}_{-24}	$14.7^{+0.3}_{-0.3}$	$3.98^{+0.73}_{-0.80}$	Seis, with dist
67	Kepler 9407261	1.57 ± 0.02	9.89 ± 0.48	8.30 ± 0.04	0.74 ± 0.01	3794^{+51}_{-54}	$20.1^{+0.5}_{-0.5}$	$5.56^{+1.81}_{-1.04}$	Seis, with dist
68	Kepler 9583607	3.83 ± 0.03	25.25 ± 0.51	8.03 ± 0.01	0.66 ± 0.01	1590^{+11}_{-12}	$9.9^{+0.2}_{-0.2}$	$12.24^{+2.29}_{-1.25}$	Indi, with dist
69	Kepler 9595645	0.94 ± 0.01	5.95 ± 0.42	8.07 ± 0.01	0.72 ± 0.01	1771^{+21}_{-21}	$33.1^{+0.6}_{-0.6}$	$1.40^{+0.33}_{-0.20}$	Seis, with dist
70	Kepler 5446927	2.91 ± 0.03	21.88 ± 0.38	7.85 ± 0.01	0.87 ± 0.01	2186^{+385}_{-107}	$13.2^{+1.8}_{-1.4}$	$4.90^{+7.37}_{-3.25}$	Indi, w/o dist

[a]Evolutionary phase changed to RC.
[b]*K2* GAP seismology.
[c]Evolutionary phase changed to RGB.

Table A2. Table of stellar sample. INDEX and ID as in Table A1. Probability of stars being *ex situ* and GES star with 0.1 dex error (01) and with APOGEE given error and the classification based on the (01) probabilities.

INDEX	ID	*P*(*Ex situ*) (01)	*P*(*Ex situ*)	*P*(GES) (01)	*P*(GES)	Classification
1	K2C1 201609020	0.74	0.87	0.00	0.00	*Ex situ*
2	K2C1 201709805	1.00	1.00	0.21	0.66	*Ex situ*/GES
3	K2C3 205934106	0.96	1.00	0.00	0.00	*Ex situ*
4	K2C3 206516677	0.77	1.00	0.33	0.99	*Ex situ*/GES
5	K2C4 211001845	1.00	1.00	0.54	0.99	*Ex situ*/GES
6	K2C6 212319585	0.94	0.94	0.00	0.00	*Ex situ*
7	K2C7 213616808	0.89	0.97	0.01	0.00	*Ex situ*
8	K2C8 220238966	0.87	1.00	0.43	0.91	*Ex situ*/GES
9	Kepler 10083815	0.79	1.00	0.00	0.00	*Ex situ*
10	Kepler 10460723	0.88	1.00	0.00	0.00	*Ex situ*
11	Kepler 11563791	0.67	0.99	0.00	0.00	*Ex situ*
12	Kepler 11566038	0.97	0.98	0.00	0.00	*Ex situ*
13	Kepler 12111110	0.79	0.92	0.47	0.82	*Ex situ*/GES
14	Kepler 12253381	1.00	1.00	0.24	0.50	*Ex situ*/GES
15	Kepler 2971380	0.81	0.94	0.39	0.89	*Ex situ*/GES
16	Kepler 4143467	0.97	1.00	0.00	0.00	*Ex situ*
17	Kepler 5953450	0.95	0.99	0.05	0.00	*Ex situ*
18	Kepler 6865157	0.79	1.00	0.00	0.00	*Ex situ*
19	Kepler 7948268	0.92	1.00	0.00	0.00	*Ex situ*
20	Kepler 8694070	0.88	0.90	0.46	0.79	*Ex situ*/GES
21	Kepler 9339711	0.99	1.00	0.00	0.00	*Ex situ*
22	K2C11 204785972	0.00	0.00	0.00	0.00	*In situ*
23	K2C17 251512185	0.00	0.00	0.00	0.00	*In situ*
24	K2C2 204298932	0.00	0.00	0.00	0.00	*In situ*
25	K2C2 205083494	0.00	0.00	0.00	0.00	*In situ*
26	K2C3 205972576	0.00	0.00	0.00	0.00	*In situ*
27	K2C3 205997746	0.00	0.00	0.00	0.00	*In situ*
28	K2C3 206011766	0.00	0.00	0.00	0.00	*In situ*
29	K2C6 212297999	0.00	0.00	0.00	0.00	*In situ*
30	K2C7 213463719	0.00	0.00	0.00	0.00	*In situ*
31	K2C7 213523425	0.00	0.00	0.00	0.00	*In situ*
32	K2C7 213532050	0.00	0.00	0.00	0.00	*In situ*
33	K2C7 213632986	0.00	0.00	0.00	0.00	*In situ*
34	K2C7 213764390	0.00	0.00	0.00	0.00	*In situ*
35	K2C7 213840500	0.00	0.00	0.00	0.00	*In situ*
36	K2C7 213853964	0.00	0.00	0.00	0.00	*In situ*
37	K2C8 220269276	0.00	0.00	0.00	0.00	*In situ*
38	K2C8 220387868	0.00	0.00	0.00	0.00	*In situ*
39	Kepler 10096113	0.00	0.00	0.00	0.00	*In situ*
40	Kepler 10207078	0.00	0.00	0.00	0.00	*In situ*
41	Kepler 10398120	0.00	0.00	0.00	0.00	*In situ*
42	Kepler 10992126	0.00	0.00	0.00	0.00	*In situ*
43	Kepler 11037292	0.00	0.00	0.00	0.00	*In situ*
44	Kepler 11774651	0.00	0.00	0.00	0.00	*In situ*
45	Kepler 12109442	0.00	0.00	0.00	0.00	*In situ*
46	Kepler 12506245	0.00	0.00	0.00	0.00	*In situ*
47	Kepler 1726211	0.00	0.00	0.00	0.00	*In situ*
48	Kepler 2165615	0.00	0.00	0.00	0.00	*In situ*
49	Kepler 2301577	0.00	0.00	0.00	0.00	*In situ*
50	Kepler 2444790	0.00	0.00	0.00	0.00	*In situ*
51	Kepler 2571323	0.00	0.00	0.00	0.00	*In situ*
52	Kepler 2714397	0.00	0.00	0.00	0.00	*In situ*

Table A2 – *continued*

INDEX	ID	*P*(*Ex situ*) (01)	*P*(*Ex situ*)	*P*(GES) (01)	*P*(GES)	Classification
53	Kepler 2831815	0.00	0.00	0.00	0.00	*In situ*
54	Kepler 5371173	0.00	0.00	0.00	0.00	*In situ*
55	Kepler 5698156	0.00	0.00	0.00	0.00	*In situ*
56	Kepler 5792889	0.00	0.00	0.00	0.00	*In situ*
57	Kepler 6267115	0.00	0.00	0.00	0.00	*In situ*
58	Kepler 7191496	0.02	0.03	0.00	0.00	*In situ*
59	Kepler 7502070	0.00	0.00	0.00	0.00	*In situ*
60	Kepler 7596219	0.00	0.00	0.00	0.00	*In situ*
61	Kepler 7908109	0.00	0.00	0.00	0.00	*In situ*
62	Kepler 7946809	0.00	0.00	0.00	0.00	*In situ*
63	Kepler 8350894	0.11	0.11	0.02	0.04	*In situ*
64	Kepler 8411446	0.00	0.00	0.00	0.00	*In situ*
65	Kepler 8544630	0.00	0.00	0.00	0.00	*In situ*
66	Kepler 9405480	0.00	0.00	0.00	0.00	*In situ*
67	Kepler 9407261	0.21	0.00	0.00	0.00	*In situ*
68	Kepler 9583607	0.00	0.00	0.00	0.00	*In situ*
69	Kepler 9595645	0.00	0.00	0.00	0.00	*In situ*
70	Kepler 5446927	0.30	0.33	0.00	0.00	*In situ*

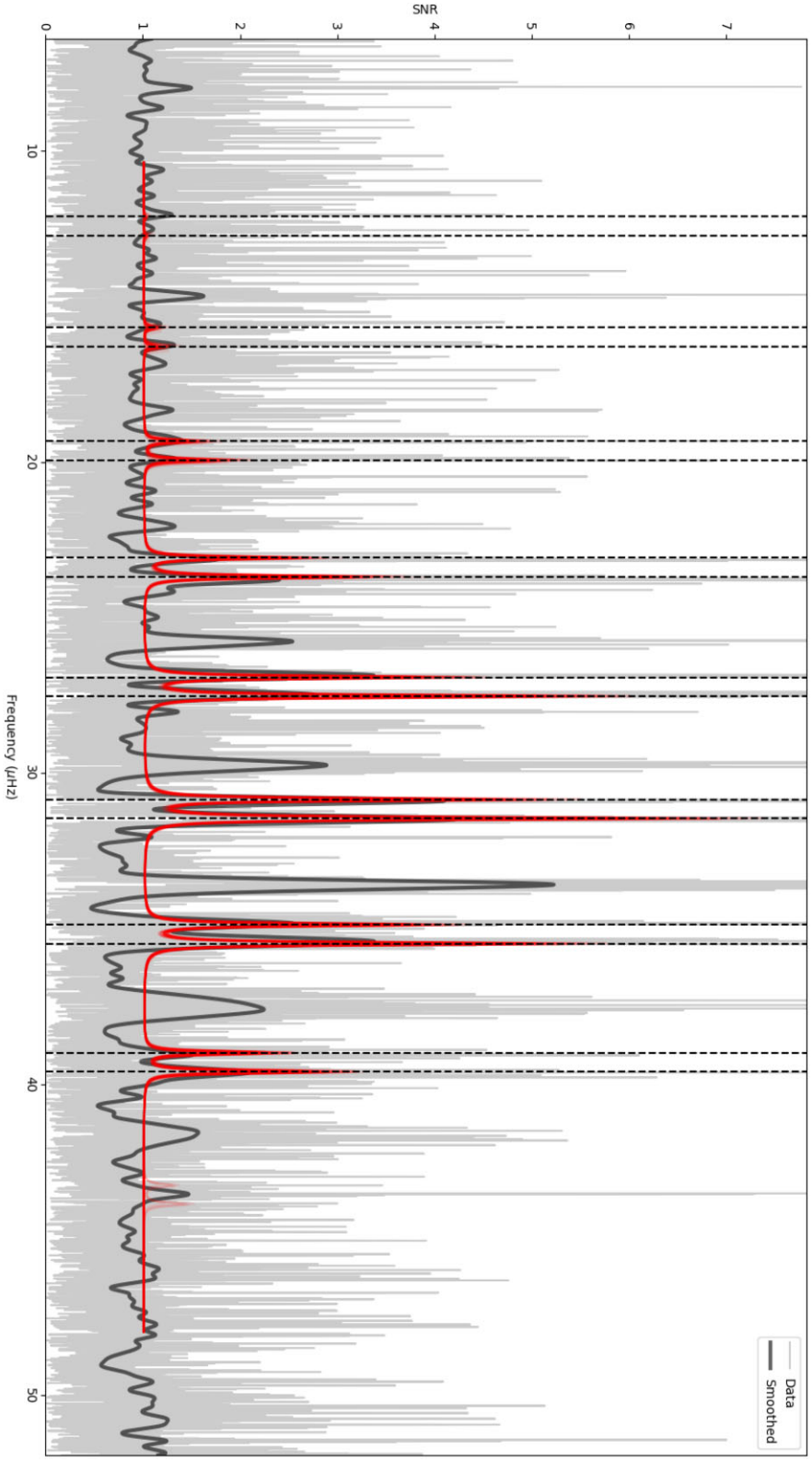

Figure A1. Example of power spectrum and peak bagging produced with PBJAM. The power spectrum is for #12 or KIC11566038.

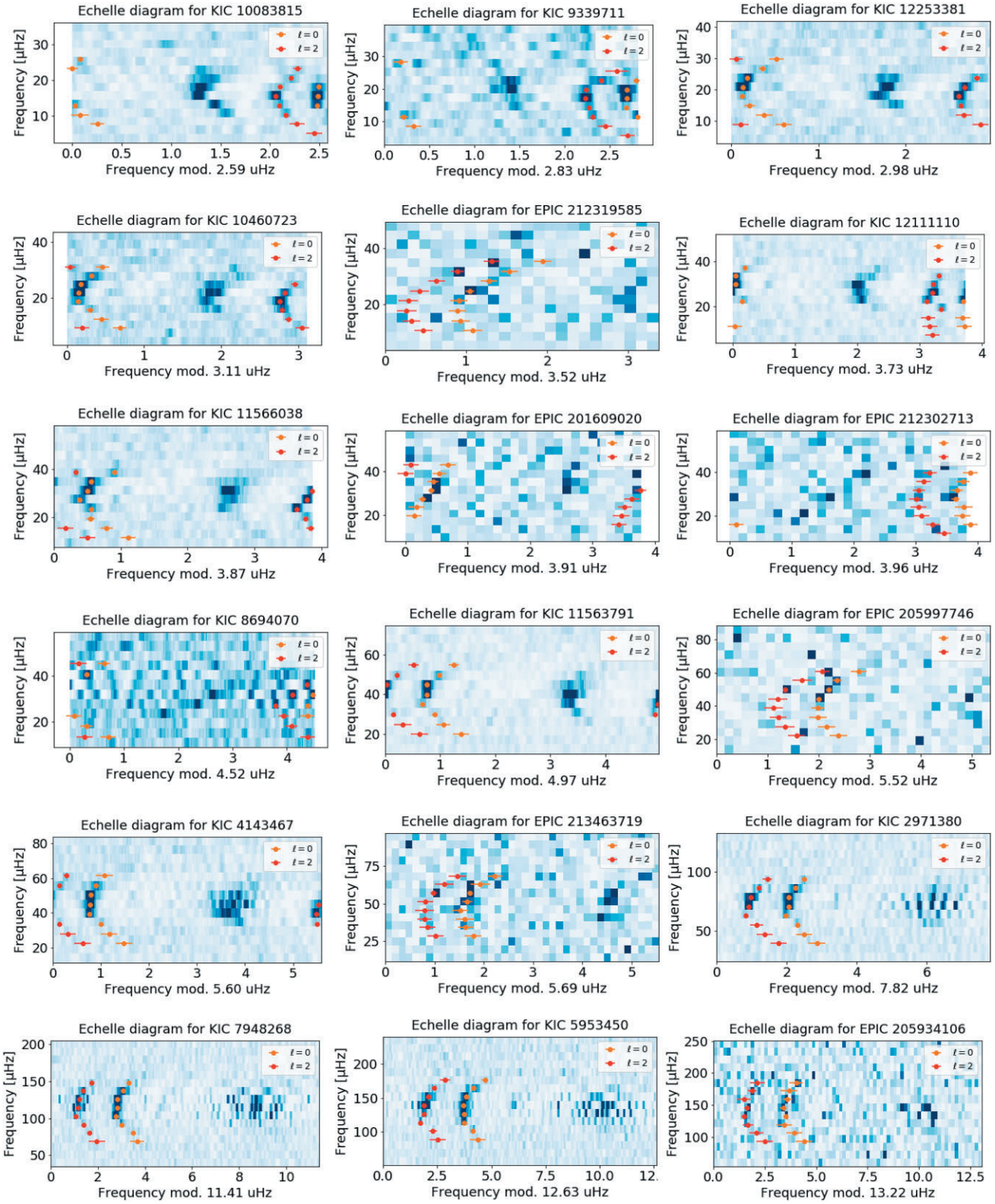

Figure A2. Echelle diagrams for a selection of targets presented in Table A1. KIC refers to *Kepler* stars and EPIC to *K2* stars.

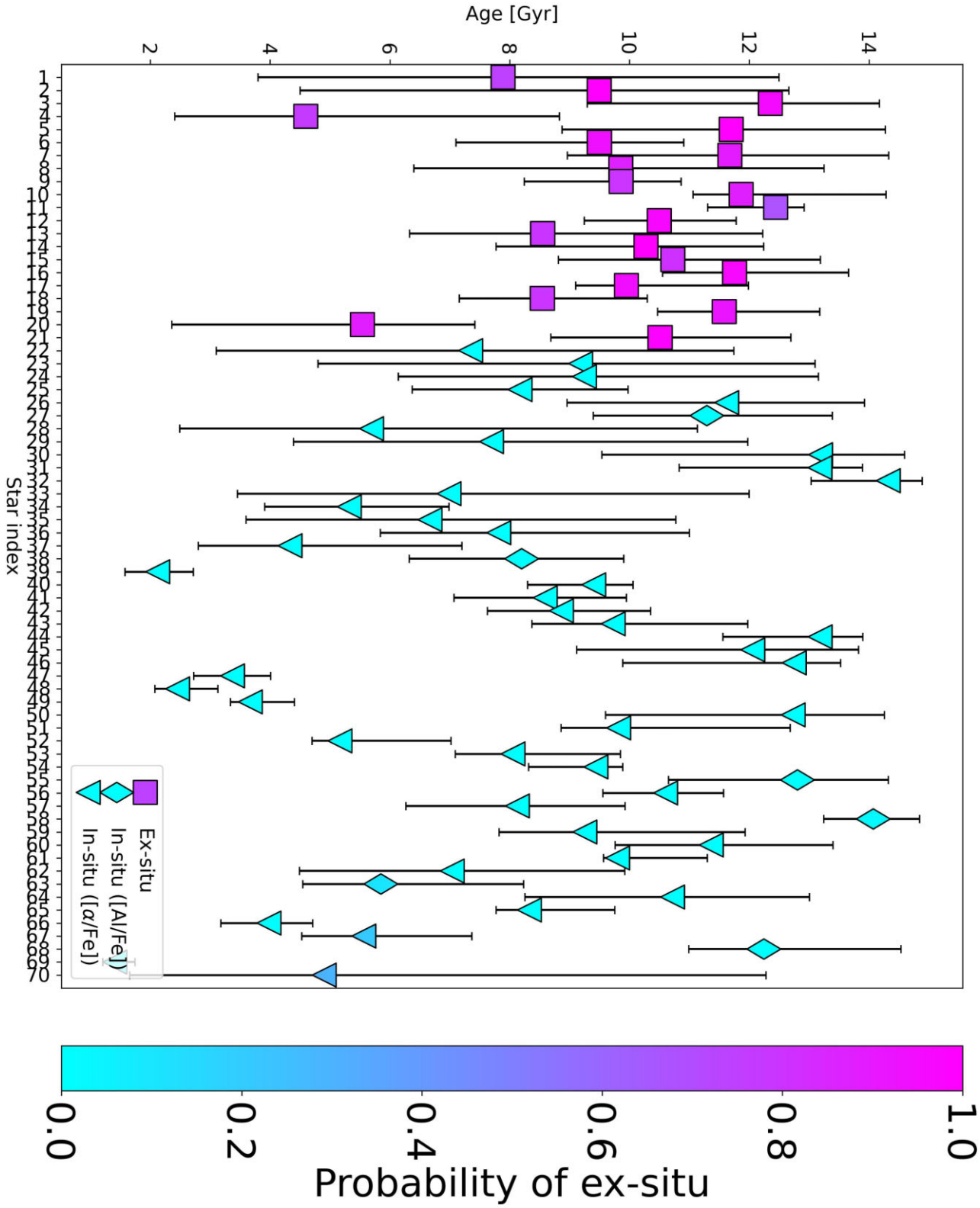

Figure A3. Ages of the stars with uncertainties. Indices match the ones used in other figures. Symbols are explained in Section 3 and colour correspond to membership probability of *ex situ* stars calculated with 0.1 dex uncertainties in [Fe/H] and [α/Fe].

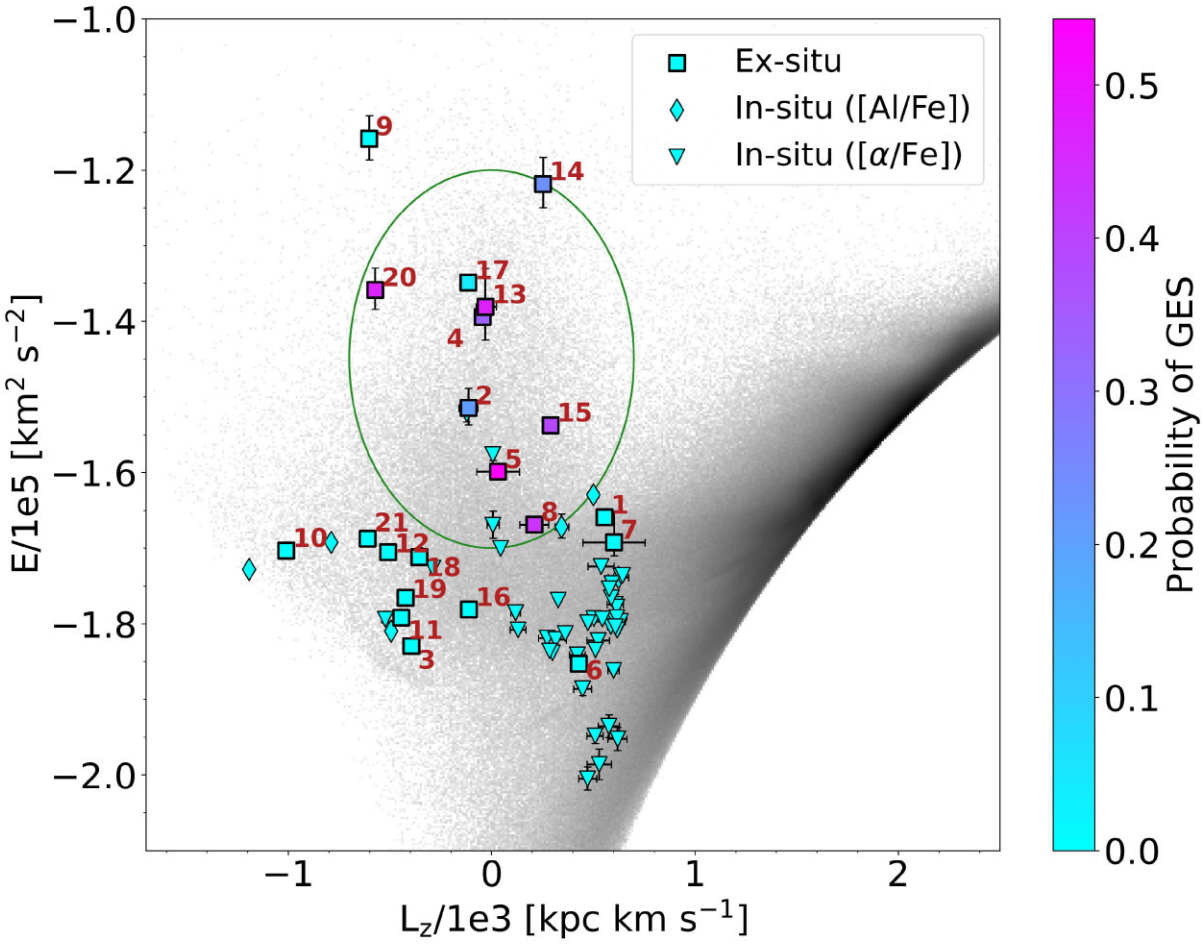

Figure A4. Similar to Fig. 2 but with only *ex situ* stars colour coded according to membership probability of GES.

This paper has been typeset from a TEX/LATEX file prepared by the author.